

Discontinuous Galerkin finite element method for shallow two-phase flows

S. Rhebergen*, O. Bokhove and J.J.W. van der Vegt

*Department of Applied Mathematics, University of Twente, P.O. Box 217, 7500
AE, Enschede, The Netherlands*

Abstract

We present a discontinuous Galerkin finite element method for two depth-averaged two-phase flow models. One of these models contains nonconservative products for which we developed a discontinuous Galerkin finite element formulation in Rhebergen *et al.* (2008) *J. Comput. Phys.* **227**, 1887-1922. The other model is a new depth-averaged two-phase flow model we introduce for shallow two-phase flows that does not contain nonconservative products. We will compare numerical results of both models and qualitatively validate the models against a laboratory experiment. Furthermore, because of spurious oscillations that may occur near discontinuities, a WENO slope limiter is applied in conjunction with a discontinuity detector to detect regions where spurious oscillations appear.

Key words: discontinuous Galerkin finite element methods, multiphase flows, nonconservative products, slope limiter, discontinuity detector

PACS: 02.60.Cb, 02.70.Dh, 47.55.-t

1991 MSC: 35L65, 35Q35, 65M60, 76M10, 76T99

1 Introduction

Debris flows are flows of water-saturated slurry mixtures (Iverson and Denlinger [17], Major and Iverson [26], Pitman and Le [29]). Examples are mud slides initiated by heavy rainfall on eroded mountain sides consisting of mixtures of rock, sand and mud; and volcanic debris flows in which the flow may

* Corresponding author. Tel.: +31 (0)53 4893415; fax: +31 (0)53 4894833

Email addresses: rhebergens@math.utwente.nl (S. Rhebergen),

o.bokhove@math.utwente.nl (O. Bokhove),

j.j.w.vandervegt@math.utwente.nl (J.J.W. van der Vegt).



(a) A lahar following a moderate eruption from Volcán Tungurahua [21].



(b) Slurry and sediment transport in pipelines [33].

Fig. 1. Examples of two-phase flows.

be a mixture of volcanic debris and water (see Fig. 1a). These flows often cause major destruction to buildings and infrastructure, with accompanying loss of human lives.

In industrial applications, dense liquid-solid flows, such as slurry flows, are used in pipeline transportation (see Fig. 1b). This form of transportation has relatively low operation and maintenance costs, and is friendly to the environment (Ling et al. [24]). Other applications occur in liquid fluidized beds (Jackson [18]).

The most common three dimensional continuum model to simulate two-phase flow in literature is a model derived in e.g. Drew and Lahey [11], Drew and Passman [12], Enwald et al. [13] and Jackson [18]. Following the literature, we call this model Model A. A modified model, Model B, was presented by the IIT/ANL group (Gidaspow [14]) (see Appendix A for Models A and B). The reason why Model B was introduced is because Model A is only conditionally hyperbolic while Model B is unconditionally hyperbolic. In liquid-solid flows, Model A is hyperbolic only for very high particle volume fractions making it less suitable for liquid-solid flows. The difference between models A and B is that in Model B the liquid pressure occurs only in the liquid momentum equation while in Model A the liquid pressure occurs in both the liquid and solids momentum equations. The mixture momentum equations, however, for both models are identical. Most researchers considering gas-solid two-phase flows however prefer Model A [13], because it is physically more correct [5,18], but as mentioned by Gidaspow [14], the models are expected to give a different value of the relative velocity only and not for the average mixture quantities.

In many flows the height H of the flow is much smaller than the length L of the flow, $H/L \ll 1$. For these flows, depth-averaging techniques are commonly

used to simplify the three dimensional equations. Examples include the shallow water equations derived from the incompressible Navier-Stokes equations or the Savage-Hutter equations for dry granular flow (Savage and Hutter [32]). Recently, Pitman and Le [29] and Le [22] derived a depth-averaged model for two-phase flows based on the three dimensional model Model A. We will call this model depth averaged model A. In this article we will present a new depth-averaged model for two-phase flows, but we base the depth-averaging on Model B. We will call this model depth-averaged model B. Unlike depth-averaged model A, depth-averaged model B can be written in flux conservative form. Although Model B is unconditionally hyperbolic, the depth-averaged model B is only conditionally hyperbolic due to the depth-averaging process. We will see, however, that depth-averaged model B is hyperbolic for a larger range of parameters than depth-averaged model A.

For the depth-averaged two-phase flow models, we present a discontinuous Galerkin finite element method (DGFEM). Among other advantages, DGFEM is a very local scheme making it well suitable to use for complicated geometries. Furthermore, the DGFEM easily deals with shocks and other discontinuities in the solution. The difficulty in the depth-averaged two-phase flow model A is the presence of nonconservative products so that this model cannot be written in flux conservative form. This causes problems once the solution becomes discontinuous, because the weak solution in the classical sense of distributions then does not exist. Consequently, no classical Rankine-Hugoniot shock conditions can be defined. We overcame these problems in Rhebergen et al. [31], where we introduced a discontinuous Galerkin finite element method and a new numerical flux, the NCP flux, for hyperbolic partial differential equations containing nonconservative products which is based on the theory by Dal Maso, LeFloch and Murat (DLM) [9], which we also apply here. As mentioned above, we will also introduce a new depth-averaged two-phase flow model, based on Model B. This new depth-averaged two-phase flow model does not contain nonconservative products so that standard DGFEM can be applied to this model. We will compare both models by comparing numerical results.

The DGFEM does not guarantee monotone solutions around discontinuities and sharp gradients and thus spurious numerical oscillations develop. To prevent these numerical oscillations we apply the WENO slope limiter given in [25] in combination with Krivodonova's discontinuity detector [20].

Much of the research conducted with depth averaged models for liquid-solid flows focuses on correctly predicting the final depositions of debris avalanches and their behavior over natural terrains (Denlinger and Iverson [10], Patra et al. [27,28], Pouliquen and Forterre [30], Tai et al. [34], Wang et al. [39]). In Chiou et al. [7] and Gray et al. [15] the influence of obstacles on granular flows is investigated. We are, however, interested in the behavior of debris

flows through contractions and in this article we will perturb a steady-state two-phase flow with a low particle volume fraction by introducing an upstream avalanche of particles for a short period, thus temporarily increasing the particle volume fraction. This experiment was done by Akers and Bokhove [1] (see Fig. 2) and we use this experiment to qualitatively validate the depth-averaged two-phase flow models. Experimental data are also available for dry granular flow through a contraction (Vreman et al. [38]). We are planning to conduct new experiments to obtain data for liquid-solid flows through a contraction with which the numerical data may be compared in the future.

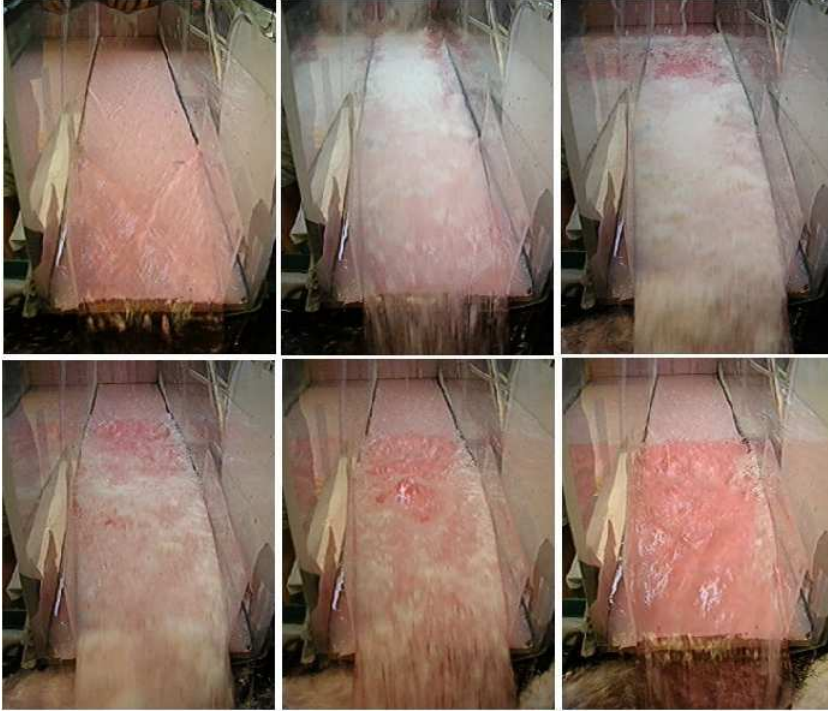


Fig. 2. The steady state with oblique hydraulic jumps (top left) is perturbed by an avalanche of polystyrene beads to an upstream steady shock state (bottom right) [1]. One second elapses between each frame.

The novelties in this article are the following:

- (1) A discontinuous Galerkin finite element discretization of the depth-averaged two-phase flow model using the theory of nonconservative products developed in [31].
- (2) Application of the WENO slope limiter [25] with Krivodanova's discontinuity detector [20] in a discontinuous Galerkin finite element discretization for two-phase flows.
- (3) Two dimensional numerical test cases of depth-averaged two-phase flow models.
- (4) A new depth-averaged two-phase flow model which can be written in flux conservative form which will be compared to the existing two-phase flow

- model [22].
- (5) Qualitative validation of the depth-averaged two-phase flow models with laboratory data.

The outline of this article is as follows. In Section 2 we present the depth-averaged model as derived by Pitman and Le [29] and Le [22] as well as a new depth-averaged two-phase flow model. We continue in Section 3 to introduce the discontinuous Galerkin finite element method for the model; numerical verification and validation is discussed in Sections 4 and 5. Conclusions are drawn in Section 6.

2 Depth-averaged two-phase flows

In shallow flows, the characteristic height H of the flow is typically much smaller than its characteristic length L , $H/L = \varepsilon \ll 1$. Variations in the vertical are small and we can simplify the governing equations by averaging the flow over the depth. In doing so, depth-averaged quantities are assumed to be independent of the vertical coordinate, at leading order in ε . In this section we introduce the depth-averaged two-phase flow equations derived by Le [22]. Note that the depth-averaged two-phase flow equations derived by Le [22] are slightly different from the depth-averaged two-phase flow equations derived by Pitman and Le [29]. The difference is that the momentum of the mixture of the Le model can be written in flux conservative form, while this is not the case for the momentum of the mixture of the Pitman and Le model. We will also introduce a new depth-averaged two-phase flow model based on Model B (see Appendix A for Models A and B).

Le [22] derived a depth-averaged flow model by depth-averaging the three-dimensional model Model A. In compact form, the scaled non-dimensional depth-averaged flow model is:

$$U_{i,t} + F_{ik,k} + G_{ikr}V_{r,k} = S_i, \quad i, r = 1, \dots, 6, \quad k = 1, 2. \quad (1)$$

Note that $G_{ikr}V_{r,k}$ is a nonconservative product. In (1) $U = [h(1-\alpha), h\alpha, h\alpha v_i, h(1-\alpha)u_i]^T$, $V = [h, \alpha, v_i, u_i]^T$ and

$$F_k = \begin{bmatrix} h(1-\alpha)u_k \\ h\alpha v_k \\ h\alpha v_i v_k + \varepsilon(1-\rho)\varphi_{ik}\alpha\frac{1}{2}g_3h^2 \\ h(1-\alpha)u_i u_k \end{bmatrix}, \quad G_k = \begin{bmatrix} 0 & 0 & 0 & 0 \\ 0 & 0 & 0 & 0 \\ \varepsilon\rho\alpha g_3 h & 0 & 0 & 0 \\ \varepsilon(1-\alpha)g_3 h & 0 & 0 & 0 \end{bmatrix},$$

$$S = \begin{bmatrix} 0 \\ 0 \\ (1-\rho)(-\varepsilon\varphi_{ik}\partial_k b + \varphi_{i3})\alpha g_3 h + h F_i^D + g_i h\alpha - \varepsilon\rho\alpha g_3 \partial_i b \\ -\varepsilon(1-\alpha)g_3 h \partial_i b - h F_i^D/\rho + h(1-\alpha)g_i \end{bmatrix}.$$

Depth-averaging Model B in the same way as the Le [22] depth-averaged Model A, we obtain a new depth-averaged two-phase flow model without nonconservative products:

$$U_{i,t} + \mathcal{F}_{ik,k} = S_i, \quad i = 1, \dots, 6, \quad k = 1, 2, \quad (2)$$

in which

$$U = \begin{bmatrix} h(1-\alpha) \\ h\alpha \\ h\alpha v_i \\ h(1-\alpha)u_i \end{bmatrix}, \quad \mathcal{F}_k = \begin{bmatrix} h(1-\alpha)u_k \\ h\alpha v_k \\ h\alpha v_i v_k + \varepsilon(1-\rho)\varphi_{ik}\alpha\frac{1}{2}g_3h^2 \\ h(1-\alpha)u_i u_k + \delta_{ik}\varepsilon g_3\frac{1}{2}h^2 \end{bmatrix},$$

$$S = \begin{bmatrix} 0 \\ 0 \\ (1-\rho)(-\varepsilon\varphi_{ik}\partial_k b + \varphi_{i3})\alpha g_3 h + h F_i^D/(1-\alpha) + (1-\rho)g_i h\alpha \\ -\varepsilon g_3 h \partial_i b - h F_i^D/(\rho(1-\alpha)) + h g_i \end{bmatrix}.$$

As with the three dimensional models A and B, the momentum equations of the separate phases in (1) and (2) are different, but the mixture momentum equations for both models are the same (see also Appendix A).

In the above models, the depth averaged quantities are: α the particle volume fraction, u the fluid velocity vector, v the solids velocity vector. The flow depth is given by h and the bottom topography by b . The constants $\varepsilon = H/L$ and $\rho = \rho^f/\rho^s$ represent the height to length ratio of the flow and the ratio between the fluid density ρ^f and the solids density ρ^s , respectively. The grav-

ity vector is given by g .

A closure needs to be given for the drag function F^D and we follow Pitman and Le [29] by taking $F_i^D = \beta(u_i - v_i)$ in which β is given by:

$$\beta = \frac{(1 - \rho)\alpha}{v_T(1 - \alpha)^n}, \quad n = \begin{cases} 3.65 & \text{for } Re_t < 0.2, \\ 4.35Re_t^{-0.03} - 1 & \text{for } 0.2 < Re_t < 1, \\ 4.45Re_t^{-0.1} - 1 & \text{for } 1 < Re_t < 500, \\ 1.39 & \text{for } 500 < Re_t, \end{cases}$$

where $Re_t = d\rho_f v_T / \mu_f$, in which d is the particle diameter, ρ^f the fluid density, μ_f the fluid viscosity and v_T the terminal velocity of an isolated particle falling in the fluid. We remark that as $1 - \rho$ increases, the drag function F^D makes the systems (1) and (2) increasingly stiffer. We are, however, interested in the case where ρ is approximately 0.9. In this situation the model does not have stiff source terms and no special algorithms are needed to deal with stiffness.

The functions φ were introduced by Pitman and Le [29] to relate basal and diagonal shear stresses to the normal stress in the solids phase stress tensor in the 3-dimensional two-phase model before depth-averaging. The functions φ are given by:

$$\begin{aligned} \varphi_{i3} &= -\frac{v_i}{\|v\|} \tan(\phi_{bed}), \quad i = 1, 2, & \varphi_{ii} &= k^\mp, \quad i = 1, 2 \\ \varphi_{12} &= -\text{sign}(\partial_2 v_1) \sin(\phi_{int}) k^\mp, & \varphi_{21} &= -\text{sign}(\partial_1 v_2) \sin(\phi_{int}) k^\mp, \\ k^\mp &= 2 \frac{1 \mp \sqrt{1 - \cos^2(\phi_{int})(1 + \tan^2(\phi_{bed}))}}{\cos^2(\phi_{int})} - 1, \end{aligned}$$

in which the “−” in the “ \mp ” applies when $\partial_k v_k > 0$ and the “+” applies when $\partial_k v_k < 0$. Furthermore, $\|\cdot\|$ is the Euclidean norm, ϕ_{int} is the internal angle of friction, which measures how layers of solid particles slide over one another and ϕ_{bed} is the basal angle of friction, indicating how easily solid particles slide over the bottom.

To determine whether the depth averaged models are hyperbolic, we need to determine their eigenvalues. If all eigenvalues are real and distinct, the model is hyperbolic. Deriving the eigenvalues for the depth-averaged models is not trivial, so eigenvalues are computed numerically for a number of given parameters. We take $b = 0$, $h = 1$, $\rho = 0.9$, $g_3 = 1$ and we assume $k^\mp = k^-$. Furthermore, we take $\phi_{bed} = 14.75^\circ$ and $\phi_{int} = 24.5^\circ$ which hold for fine glass particles [4]. For different height to length ratios, ranging from $\varepsilon = 0.001$ to $\varepsilon = 1$, we determine the eigenvalues as a function of the particle volume fraction α and the absolute difference between the phase velocities $|u - v|$. In Figure 3 we show for which values of α and $|u - v|$ the depth-averaged

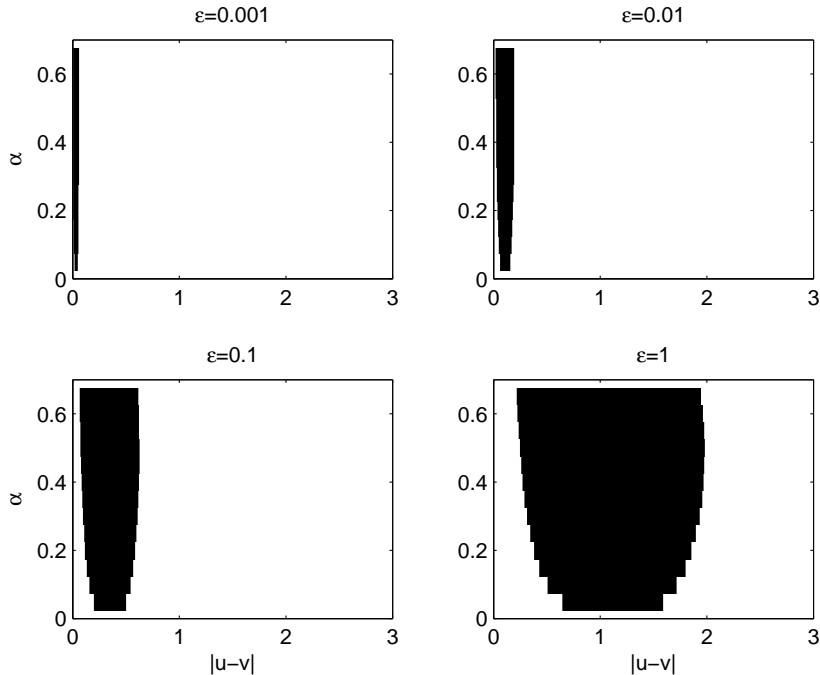


Fig. 3. Regimes of hyperbolicity for depth-averaged model A. For the values of α and $|u - v|$ in the shaded area the model is elliptic.

Model A is not hyperbolic (for the parameters in the shaded areas some of the eigenvalues are not real) while in Figure 4 we show this for depth-averaged Model B. For both models we see that the region for which the model is not hyperbolic decreases as ε decreases. We also see that depth-averaged model B is hyperbolic for a larger range of α and $|u - v|$ values than depth-averaged model A. In this article we are only interested in cases where the model is hyperbolic. When the model is not hyperbolic, a different numerical approach needs to be introduced which is not treated in this article.

3 The DGFEM discretization

In this section we present a space-time DGFEM formulation for depth-averaged two-phase flow models. We remark however that the space DGFEM formulation is very similar and for some of the numerical test cases we will apply space DGFEM. For more on space DGFEM we refer to Rhebergen et al. [31] and Cockburn and Shu [8].

We start by introducing space-time elements, function spaces, trace operators and basis functions after which we present the space-time DGFEM formulation for the depth-averaged two-phase flow models.

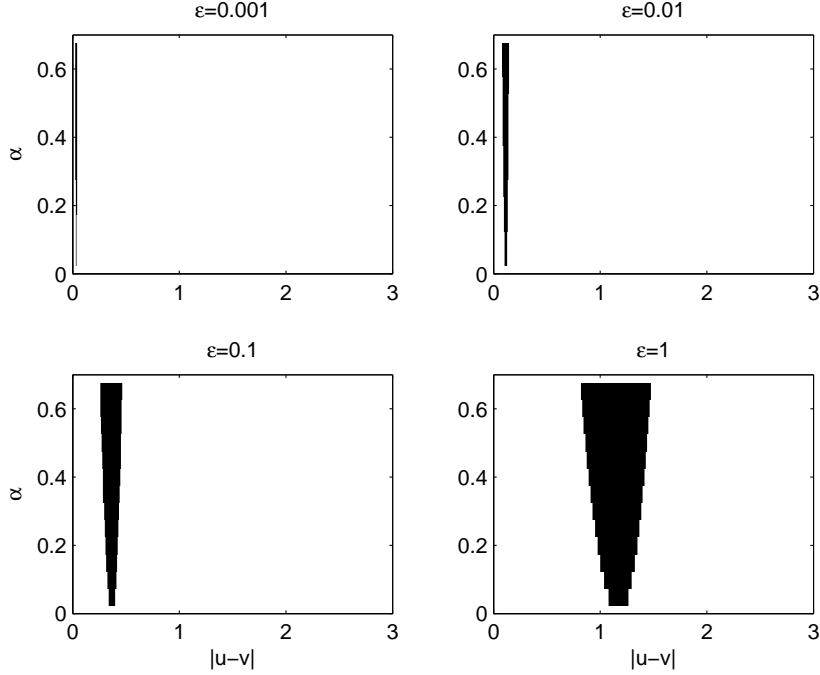


Fig. 4. Regimes of hyperbolicity for depth-averaged model B. For the values of α and $|u - v|$ in the shaded area the model is elliptic.

3.1 Space-time elements

In the space-time DGFEM method, the space and time variables are treated together. A point at time $t = x_0$ with position vector $\bar{x} = (x_1, x_2)$ has Cartesian coordinates (x_0, \bar{x}) in the open domain $\mathcal{E} \subset \mathbb{R}^3$. At time t , the flow domain $\Omega(t)$ is defined as:

$$\Omega(t) := \{\bar{x} \in \mathbb{R}^2 : (t, \bar{x}) \in \mathcal{E}\}.$$

By taking t_0 and T as the initial and final time of the evolution of the space-time flow domain, the space-time domain boundary $\partial\mathcal{E}$ consists of the hyper-surfaces:

$$\begin{aligned} \Omega(t_0) &:= \{x \in \partial\mathcal{E} : x_0 = t_0\}, \\ \Omega(T) &:= \{x \in \partial\mathcal{E} : x_0 = T\}, \\ \mathcal{Q} &:= \{x \in \partial\mathcal{E} : t_0 < x_0 < T\}. \end{aligned}$$

The time interval $[t_0, T]$ is partitioned using the time levels $t_0 < t_1 < \dots < T$, where the n -th time interval is defined as $I_n = (t_n, t_{n+1})$ with length $\Delta t_n = t_{n+1} - t_n$. The space-time domain \mathcal{E} is then divided into N_t space-time slabs $\mathcal{E}^n = \mathcal{E} \cap I_n$. Each space-time slab \mathcal{E}^n is bounded by $\Omega(t_n)$, $\Omega(t_{n+1})$ and $\mathcal{Q}^n = \partial\mathcal{E}^n / (\Omega(t_n) \cup \Omega(t_{n+1}))$.

The flow domain $\Omega(t_n)$ is approximated by $\Omega_h(t_n)$, where $\Omega_h(t) \rightarrow \Omega(t)$

as $h \rightarrow 0$, with h the radius of the smallest sphere completely containing the largest space-time element. The domain $\Omega_h(t_n)$ is divided into N_n non-overlapping spatial elements $K_j(t_n)$. Similarly, $\Omega(t_{n+1})$ is approximated by $\Omega_h(t_{n+1})$. We can relate each element $K_j^n = K_j(t_n)$ to a master element $\hat{K} \subset \mathbb{R}^2$ through the mapping F_K^n :

$$F_K^n : \hat{K} \rightarrow K_j^n : \bar{\xi} \mapsto \bar{x} = \sum_i x_i(K_j^n) \chi_i(\bar{\xi})$$

with x_i the spatial coordinates of the vertices of the spatial element K_j^n and χ_i the standard Lagrangian shape functions defined on element \hat{K} . The space-time elements \mathcal{K}_j^n are constructed by connecting K_j^n with K_j^{n+1} using linear interpolation in time, resulting in the mapping $G_{\mathcal{K}}^n$ from the master element $\hat{\mathcal{K}} \subset \mathbb{R}^3$ to the space-time element \mathcal{K}^n :

$$G_{\mathcal{K}}^n : \hat{\mathcal{K}} \rightarrow \mathcal{K}^n : \xi = (\xi_0, \bar{\xi}) \mapsto (t, \bar{x}) = \left(\frac{1}{2}(t_{n+1} + t_n) + \frac{1}{2}(t_{n+1} - t_n)\xi_0, \right. \\ \left. \frac{1}{2}(1 - \xi_0)F_K^n(\bar{\xi}) + \frac{1}{2}(1 + \xi_0)F_K^{n+1}(\bar{\xi}) \right),$$

with $\xi_0 \in [-1, 1]$ and $\bar{\xi} \in \hat{K}$. The tessellation \mathcal{T}_h^n of the space-time slab \mathcal{E}_h^n consists of all space-time elements \mathcal{K}_j^n ; thus the tessellation \mathcal{T}_h of the discrete flow domain $\mathcal{E}_h := \cup_{n=0}^{N_t-1} \mathcal{E}_h^n$ then is defined as $\mathcal{T}_h := \cup_{n=0}^{N_t-1} \mathcal{T}_h^n$.

The element boundary $\partial\mathcal{K}_j^n$, the union of open faces of \mathcal{K}_j^n , consists of three parts: $K_j(t_n^+) = \lim_{\epsilon \downarrow 0} K_j(t_n + \epsilon)$, $K_j(t_{n+1}^-) = \lim_{\epsilon \downarrow 0} K_j(t_{n+1} - \epsilon)$ and $\mathcal{Q}_j^n = \partial\mathcal{K}_j^n / (K_j(t_n^+) \cup K_j(t_{n+1}^-))$. The outward space-time normal vector on $\partial\mathcal{K}_j^n$ is given by:

$$n = \begin{cases} (1, \bar{0}) & \text{at } K_j(t_{n+1}^-), \\ (-1, \bar{0}) & \text{at } K_j(t_n^+), \\ (0, \bar{n}) & \text{at } \mathcal{Q}_j^n, \end{cases} \quad (3)$$

where $\bar{0} \in \mathbb{R}^2$. It is convenient to split the element boundaries into separate faces. In addition to faces $K_j(t_n^+)$ and $K_j(t_{n+1}^-)$, we also define therefore interior and boundary faces. An interior face is shared by two neighboring elements \mathcal{K}_i^n and \mathcal{K}_j^n , such that $\mathcal{S}_{ij}^n = \mathcal{Q}_i^n \cap \mathcal{Q}_j^n$; a boundary face is defined as $\mathcal{S}_{Bj}^n = \partial\mathcal{E}^n \cap \mathcal{Q}_j^n$. The set of interior faces in a space-time slab \mathcal{E}^n is denoted by \mathcal{S}_I^n and the set of all boundary faces by \mathcal{S}_B^n ; the total set is denoted by $\mathcal{S}_{I,B}^n = \mathcal{S}_I^n \cup \mathcal{S}_B^n$.

3.2 Function spaces and trace operators

We consider approximations of $U(x, t)$ and functions $W(x, t)$ in the finite element space W_h defined as:

$$W_h = \left\{ W \in (L^2(\mathcal{E}_h))^m : W|_{\mathcal{K}} \circ G_{\mathcal{K}} \in (P^p(\hat{\mathcal{K}}))^m, \forall \mathcal{K} \in \mathcal{T}_h \right\},$$

where $L^2(\mathcal{E}_h)$ is the space of square integrable functions on \mathcal{E}_h and $P^p(\hat{\mathcal{K}})$ the space of polynomials of degree at most p on reference element $\hat{\mathcal{K}}$. Here m denotes the dimension of U . In our case, $m = 6$ and we use linear approximations with $p = 1$.

We now introduce some operators as defined in Klaij et al. [19]. The trace of a function $f \in V_h$ at the element boundary $\partial\mathcal{K}^L$ is defined as:

$$f^L = \lim_{\epsilon \downarrow 0} f(x - \epsilon n^L),$$

with n^L the unit outward space-time normal at $\partial\mathcal{K}^L$. When only the space components of the outward normal vector are considered we will use the notation \bar{n}^L . A function $f \in W_h$ has a double valued trace at element boundaries $\partial\mathcal{K}$. The traces of a function f at an internal face $\mathcal{S} = \bar{\mathcal{K}}^L \cap \bar{\mathcal{K}}^R$ are denoted by f^L and f^R . The jump of f at an internal face $\mathcal{S} \in \mathcal{S}_I^n$ in the direction k of a Cartesian coordinate system is defined as:

$$[[f]]_k = f^L \bar{n}_k^L + f^R \bar{n}_k^R,$$

with $\bar{n}_k^R = -\bar{n}_k^L$. The average of f at $\mathcal{S} \in \mathcal{S}_I^n$ is defined as:

$$\{\{f\}\} = \frac{1}{2}(f^L + f^R).$$

The jump operator satisfies the following product rule at $\mathcal{S} \in \mathcal{S}_I^n$ for $\forall l \in W_h$ and $\forall f_k \in W_h$, which can be proven by direct verification:

$$[[l_i f_{ik}]]_k = \{\{l_i\}\} [[f_{ik}]]_k + [[l_i]]_k \{\{f_{ik}\}\}. \quad (4)$$

Consequently, we can relate element boundary integrals to face integrals:

$$\sum_{\mathcal{K} \in \mathcal{T}_h^n} \int_{\mathcal{Q}} l_i^L f_{ik}^L \bar{n}_k^L d\mathcal{Q} = \sum_{\mathcal{S} \in \mathcal{S}_I^n} \int_{\mathcal{S}} [[l_i f_{ik}]]_k d\mathcal{S} + \sum_{\mathcal{S} \in \mathcal{S}_B^n} \int_{\mathcal{S}} l_i^L f_{ik}^L \bar{n}_k^L d\mathcal{S}. \quad (5)$$

3.3 Basis functions

Polynomial approximations for the trial function U and the test functions W in each element $\mathcal{K} \in \mathcal{T}_h^n$ are introduced as:

$$U(t, \bar{x})|_{\mathcal{K}} = \hat{U}_m \psi_m(t, \bar{x}) \text{ and } W(t, \bar{x})|_{\mathcal{K}} = \hat{W}_l \psi_l(t, \bar{x}), \quad (6)$$

with ψ_m the basis functions, $\bar{x} \in \mathbb{R}^2$, and expansion coefficients \hat{U}_m and \hat{W}_l , respectively, for $m, l = 0, 1, 2, 3$. The basis functions ψ_m are given by $\psi_0 = 1$ and $\psi_m = \varphi_m(t, \bar{x})$ for $m = 1, 2, 3$ where the functions $\varphi_m(x)$ in element \mathcal{K} are related to the basis functions $\hat{\varphi}_m(\xi)$, with $\hat{\varphi}_m(\xi) \in P^1(\hat{\mathcal{K}})$ and ξ the local coordinates in the master element $\hat{\mathcal{K}}$, through the mapping $G_{\mathcal{K}}: \varphi_m = \hat{\varphi}_m \circ G_{\mathcal{K}}^{-1}$.

3.4 The weak formulation

Due to the nonconservative products (1) cannot be transformed into divergence form. This causes problems once the solution becomes discontinuous, because the weak solution in the classical sense of distributions then does not exist. Consequently, standard space-time DGFEM discretizations cannot be applied. In Rhebergen et al. [31] we derived a discontinuous Galerkin finite element weak formulation for general hyperbolic equations with nonconservative products and we apply this weak formulation here as well.

We will not give the derivation of the weak formulation for (1), instead we refer to Rhebergen et al. [31]. The main criterium we posed on the weak formulation is that if the system of nonconservative partial differential equations can be transformed into conservative form, then the formulation must reduce to that for the conservative system. The weak formulation for (1) is given by:

Find a $U \in W_h$ such that for all $W \in W_h$:

$$\begin{aligned}
0 = & \sum_{\mathcal{K} \in \mathcal{T}_h^n} \int_{\mathcal{K}} \left(-W_{i,0} U_i - W_{i,k} F_{ik} + W_i G_{ikr} V_{r,k} - W_i S_i \right) d\mathcal{K} \\
& + \sum_{\mathcal{K} \in \mathcal{T}_h^n} \left(\int_{K(t_{n+1}^-)} W_i^L U_i^L dK - \int_{K(t_n^+)} W_i^L U_i^R dK \right) \\
& + \sum_{\mathcal{S} \in \mathcal{S}^n} \int_{\mathcal{S}} (W_i^L - W_i^R) \hat{P}_i^{nc} d\mathcal{S} \\
& + \sum_{\mathcal{S} \in \mathcal{S}^n} \int_{\mathcal{S}} \{W_i\} \left(\int_0^1 G_{ikr}(\phi(\tau; U^L, U^R)) \frac{\partial \phi_r}{\partial \tau}(\tau; U^L, U^R) d\tau \bar{n}_k^L \right) d\mathcal{S}.
\end{aligned} \tag{7}$$

The last term make it different from standard discontinuous Galerkin finite element formulations. It is needed to introduce a measure for the nonconservative product where U is discontinuous. Note that an extra function, $\phi(\tau; U_L, U_R)$, has been introduced to deal with the regularization of U across the discontinuity. In [31] the effect of the choice of $\phi(\tau; U_L, U_R)$ on the numerical solution was investigated. We concluded that the numerical diffusion has a regularizing effect across discontinuities, which significantly reduces the dependence of the solution on $\phi(\tau; U_L, U_R)$, so that often it does not matter in practice how $\phi(\tau; U_L, U_R)$ is chosen. We adopt a linear path: $\phi(\tau; U_L, U_R) = U_L + \tau(U_R - U_L)$. Furthermore, we use here the NCP numerical flux $\hat{P}^{nc}(U^L, U^R, v, \bar{n}^L)$ designed in [31] for systems containing nonconservative products as a generalization of

the HLL flux [36]. The NCP numerical flux $\widehat{P}^{nc}(U^L, U^R, v, \bar{n}^L)$ reads:

$$\widehat{P}_i^{nc}(U_L, U_R, v, \bar{n}^L) = \begin{cases} F_{ik}^L \bar{n}_k^L - \frac{1}{2} \int_0^1 G_{ikr}(\bar{\phi}(\tau; U_L, U_R)) \frac{\partial \bar{\phi}_r}{\partial \tau}(\tau; U_L, U_R) d\tau \bar{n}_k^L & \text{if } S_L > v, \\ \{\!\!\{ F_{ik} \}\!\!\} \bar{n}_k^L + \frac{1}{2} ((S_R - v) \bar{U}_i^* + (S_L - v) \bar{U}_i^* - S_L U_i^L - S_R U_i^R) & \text{if } S_L < v < S_R, \\ F_{ik}^R \bar{n}_k^L + \frac{1}{2} \int_0^1 G_{ikr}(\bar{\phi}(\tau; U_L, U_R)) \frac{\partial \bar{\phi}_r}{\partial \tau}(\tau; U_L, U_R) d\tau \bar{n}_k^L & \text{if } S_R < v, \end{cases} \quad (8)$$

with \bar{U}^* given by:

$$\bar{U}_i^* = \frac{S_R U_i^R - S_L U_i^L + (F_{ik}^L - F_{ik}^R) \bar{n}_k^L}{S_R - S_L} - \frac{1}{S_R - S_L} \int_0^1 G_{ikr}(\phi(\tau; U_L, U_R)) \frac{\partial \phi_r}{\partial \tau}(\tau; U_L, U_R) d\tau \bar{n}_k^L. \quad (9)$$

Note that if set $G_{ikr} = 0$ and replace F by \mathcal{F} in (7), (8) and (9) we obtain the weak formulation for (2).

The wave speeds S_L and S_R in the numerical flux are usually approximated by the minimum and maximum eigenvalues of the Jacobian matrix. The characteristic polynomial of the Jacobian matrix of depth-averaged model A, $\partial F / \partial U + G$ is $c(\lambda) = (\lambda - q_v)(\lambda - q_u)p(\lambda)$ in which $p(\lambda) = \lambda^4 + a_1\lambda^3 + a_2\lambda^2 + a_3\lambda + a_4$ and:

$$\begin{aligned} a_1 &= -2(q_u + q_v), \\ a_2 &= q_u^2 + q_v^2 + 4q_u q_v - \varepsilon g_3 h(1 - \alpha + \rho \alpha), \\ &\quad - \frac{1}{2} \varepsilon g_3 h(1 - \rho)(1 + \alpha)(\varphi_{11} n_1^2 + \varphi_{22} n_2^2 + \varphi_{12} n_1 n_2 + \varphi_{21} n_1 n_2) \\ a_3 &= -2q_u q_v (q_u + q_v) + 2q_v \varepsilon g_3 h(1 - \alpha) + 2\varepsilon \rho g_3 \alpha h q_u \\ &\quad + 2q_u (\frac{1}{2} \varepsilon g_3 h(1 + \alpha)(1 - \rho)(\varphi_{11} n_1^2 + \varphi_{22} n_2^2 + \varphi_{12} n_1 n_2 + \varphi_{21} n_1 n_2)), \\ a_4 &= q_u^2 q_v^2 - q_u^2 (\frac{1}{2} h \varepsilon g_3 (1 - \rho)(1 + \alpha)(\varphi_{11} n_1^2 + \varphi_{22} n_2^2 + \varphi_{12} n_1 n_2 + \varphi_{21} n_1 n_2)) \\ &\quad + \frac{1}{2} \varepsilon^2 g_3^2 h^2 (1 - \rho)(1 - \alpha)(\varphi_{11} n_1^2 + \varphi_{22} n_2^2 + \varphi_{12} n_1 n_2 + \varphi_{21} n_1 n_2) \\ &\quad - q_v^2 \varepsilon g_3 h(1 - \alpha) - q_u^2 \varepsilon \rho g_3 \alpha h. \end{aligned} \quad (10)$$

Two eigenvalues are $\lambda_1 = q_v$ and $\lambda_2 = q_u$. Since explicitly solving the quartic polynomial $p(\lambda) = 0$ yields rather unwieldy relations, we approximate the remaining four eigenvalues.

We approximate $p(\lambda)$ by $\tilde{p}(\lambda) = (\lambda - q^u - \mathcal{A})(\lambda - q^u + \mathcal{A})(\lambda - q^v - \mathcal{B})(\lambda - q^v + \mathcal{B})$ and expand \tilde{p} as $\tilde{p} = \lambda^4 + a_1\lambda^3 + b_2\lambda^2 + b_3\lambda + b_4$ with coefficients:

$$\begin{aligned} b_2 &= q_u^2 + q_v^2 + 4q_u q_v - (\mathcal{A}^2 + \mathcal{B}^2), \\ b_3 &= 2q_v \mathcal{A}^2 + 2q_u \mathcal{B}^2 - 2q_v q_u (q_u + q_v), \\ b_4 &= q_v^2 q_u^2 - q_u^2 \mathcal{B}^2 - q_v^2 \mathcal{A}^2 + \mathcal{A}^2 \mathcal{B}^2. \end{aligned} \quad (11)$$

Note that by choosing

$$\begin{aligned}\mathcal{A} &= \sqrt{\varepsilon g_3 h (1 - \alpha)}, \\ \mathcal{B} &= \sqrt{\frac{1}{2} h \varepsilon g_3 (1 - \rho) (1 + \alpha) (\varphi_{11} n_1^2 + \varphi_{22} n_2^2 + \varphi_{12} n_1 n_2 + \varphi_{21} n_1 n_2)},\end{aligned}\quad (12)$$

the coefficients a_i and b_i almost match. Approximate the solutions to $p(\lambda)$ now as $\lambda_{3,4} = q_u \pm \mathcal{A}$ and $\lambda_{5,6} = q_v \pm \mathcal{B}$. The error in the approximation of the roots is then proportional to $p(\lambda_{3,4}) = \mathcal{O}(\varepsilon^2)$, and $p(\lambda_{5,6}) = \mathcal{O}(\varepsilon)$.

Similarly, for depth-averaged model B, two eigenvalues of the Jacobian matrix $\partial\mathcal{F}/\partial U$ are given by $\lambda_1 = q_u$ and $\lambda_2 = q_v$ while the other four eigenvalues are approximated as $\lambda_{3,4} = q_u \pm \mathcal{C}$ and $\lambda_{5,6} = q_v \pm \mathcal{D}$ with

$$\begin{aligned}\mathcal{C} &= \sqrt{\varepsilon g_3 h}, \\ \mathcal{D} &= \sqrt{\frac{1}{2} h \varepsilon g_3 (1 - \rho) (1 + \alpha) (\varphi_{11} n_1^2 + \varphi_{22} n_2^2 + \varphi_{12} n_1 n_2 + \varphi_{21} n_1 n_2)}.\end{aligned}\quad (13)$$

As mentioned above, $\phi(\tau; U_L, U_R)$ had to be chosen and we adopted $\phi(\tau; U_L, U_R) = U_L + \tau(U_R - U_L)$. This choice of the path presents us the opportunity to exactly determine the integral due to the nonconservative product in (7):

$$\int_0^1 G_{kr}(\phi(\tau; U_L, U_R)) \frac{\partial \phi_r}{\partial \tau}(\tau; U_L, U_R) d\tau \bar{n}_k^L = \begin{bmatrix} 0 \\ 0 \\ -\varepsilon \rho g_3 \llbracket h \rrbracket \int_0^1 \alpha h d\tau \\ -\varepsilon \rho g_3 \llbracket h \rrbracket \int_0^1 \alpha h d\tau \\ -\varepsilon g_3 \llbracket h \rrbracket \int_0^1 (1 - \alpha) h d\tau \\ -\varepsilon g_3 \llbracket h \rrbracket \int_0^1 (1 - \alpha) h d\tau \end{bmatrix}, \quad (14)$$

in which

$$\begin{aligned}\int_0^1 \alpha h d\tau &= \frac{1}{3}(\alpha_L h_L + \frac{1}{2}(\alpha_R h_L + \alpha_L h_R) + \alpha_R h_R), \\ \int_0^1 (1 - \alpha) h d\tau &= \llbracket h \rrbracket - \frac{1}{3}(\alpha_L h_L + \frac{1}{2}(\alpha_R h_L + \alpha_L h_R) + \alpha_R h_R).\end{aligned}$$

3.5 Pseudo-time stepping

By replacing U and W in the weak formulation (7) by their polynomial expansions (6), a system of algebraic equations for the expansion coefficients of

U is obtained. For each physical time step, the system can be written as:

$$\mathcal{L}(\hat{U}^n; \hat{U}^{n-1}) = 0. \quad (15)$$

This system of coupled non-linear equations is solved by adding a pseudo-time derivative of the primitive variables $V = [h, \alpha, v_i, u_i]^T$ and expressing (15) in terms of V :

$$\int_{\mathcal{K}} \phi \frac{\partial U}{\partial V} d\mathcal{K} \frac{\partial \hat{V}^n}{\partial \tau} = -\mathcal{L}(\hat{V}^n; \hat{V}^{n-1}). \quad (16)$$

This relation is integrated to steady-state in pseudo-time. Following Van der Vegt and Van der Ven [37], we use the explicit Runge-Kutta method for inviscid flow with Melson correction given by:

Algorithm 1 Five-stage explicit Runge-Kutta scheme:

- (1) Initialize $\hat{Y}^0 = \hat{U}$.
- (2) For all stages $s = 1$ to 5:

$$(I + \alpha_s \lambda I) \hat{Y}^s = \hat{Y}^0 + \alpha_s \lambda (\hat{Y}^{s-1} - \mathcal{L}(\hat{Y}^{s-1}; \hat{V}^{n-1})).$$

- (3) Update $\hat{Y} = \hat{Y}^5$.

The coefficient λ is defined as $\lambda = \Delta\tau/\Delta t$, with $\Delta\tau$ the pseudo-time step and Δt the physical time step. The Runge-Kutta coefficients α_s are defined as: $\alpha_1 = 0.0797151$, $\alpha_2 = 0.163551$, $\alpha_3 = 0.283663$, $\alpha_4 = 0.5$ and $\alpha_5 = 1.0$.

3.6 Slope limiter and discontinuity detector

In numerical discretizations of the weak formulation (7), spurious oscillations generally appear near discontinuities. Using the Krivodonova discontinuity detector [20], we apply a slope limiter only near discontinuities to deal with these spurious oscillations. We use the slope limiter given in [25] which we describe briefly here for reasons of clarity.

The idea of the slope limiter is to replace the original polynomial P_0 by a new polynomial P that uses the data u_m of the midpoints of the original element in element K_k and its neighboring elements u_a , u_b , u_c and u_d . Eight polynomials are constructed, 4 Lagrange polynomials, P_i , $i = 1, 2, 3, 4$ and 4 Hermite polynomials P_i , $i = 5, 6, 7, 8$. For the Hermite polynomials we also need the physical gradient of the data in the neighboring elements at the points \vec{x} , ∇u_a , ∇u_b , ∇u_c and ∇u_d (see Fig. 5).

To construct the Lagrange polynomials consider the surface through x_m , x_a and x_b . Name the polynomial through this surface P_1 with $P_1 = \hat{P}_1^a + \hat{P}_1^b x + \hat{P}_1^c y$.

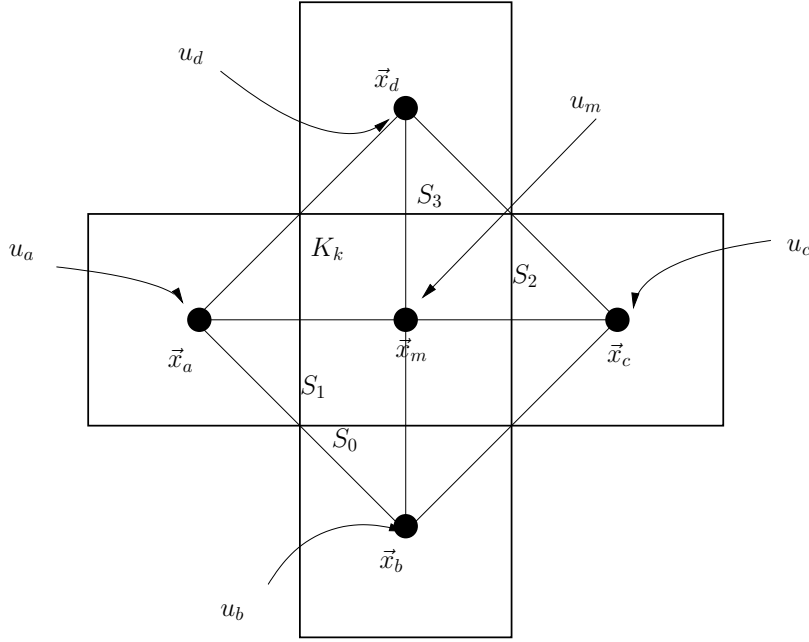


Fig. 5. Slope limiter in 2D.

The coefficients \hat{P}_1^a , \hat{P}_1^b and \hat{P}_1^c are found by solving:

$$\begin{bmatrix} 1 & x_m & y_m \\ 1 & x_a & y_a \\ 1 & x_b & y_b \end{bmatrix} \begin{bmatrix} \hat{P}_1^a \\ \hat{P}_1^b \\ \hat{P}_1^c \end{bmatrix} = \begin{bmatrix} u_m \\ u_a \\ u_b \end{bmatrix}.$$

In the same way, polynomials P_2 , P_3 and P_4 are constructed by considering the remaining three surfaces.

Each of the four Hermite polynomials are determined by looking at the current element and one of the neighbors, e.g., the first Hermite polynomial, P_5 , is found by looking at the neighboring element sharing face S_0 . In the midpoint x_b , the gradient of the solution is ∇u_b , while the solution in the midpoint of the current element is u_m . The first Hermite polynomial is given by: $P_5 = \hat{P}_5^a + \hat{P}_5^b x + \hat{P}_5^c y$ where:

$$\begin{aligned} \hat{P}_5^a &= u_m - x_b \cdot \nabla u_b, \\ \hat{P}_5^b &= \partial_x u_b \quad \text{in } x_b, \\ \hat{P}_5^c &= \partial_y u_b \quad \text{in } x_b. \end{aligned}$$

In the same way, polynomials P_6 , P_7 and P_8 are constructed by considering the remaining three surfaces.

The linear approximation of the original polynomial is determined just like the Hermite polynomials. In the midpoint x_m , the solution is u_m and the

gradient is ∇u_m . The linear approximation is: $P_0 = \hat{P}_0^a + \hat{P}_0^b x + \hat{P}_0^c y$ where:

$$\begin{aligned}\hat{P}_0^a &= u_m - x_m \cdot \nabla u_m, \\ \hat{P}_0^b &= \partial_x u_m \quad \text{in } x_m, \\ \hat{P}_0^c &= \partial_y u_m \quad \text{in } x_m.\end{aligned}$$

Now project P_j , $j = 0, \dots, 8$, onto the DG space and solve for $(\hat{u}_0)_j$, $(\hat{u}_1)_j$ and $(\hat{u}_2)_j$:

$$\begin{bmatrix} \int_{K_k} \psi_0 \psi_0 dK & \int_{K_k} \psi_0 \psi_1 dK & \int_{K_k} \psi_0 \psi_2 dK \\ \int_{K_k} \psi_1 \psi_0 dK & \int_{K_k} \psi_1 \psi_1 dK & \int_{K_k} \psi_1 \psi_2 dK \\ \int_{K_k} \psi_2 \psi_0 dK & \int_{K_k} \psi_2 \psi_1 dK & \int_{K_k} \psi_2 \psi_2 dK \end{bmatrix} \begin{bmatrix} (\hat{u}_0)_j \\ (\hat{u}_1)_j \\ (\hat{u}_2)_j \end{bmatrix} = \begin{bmatrix} \int_{K_k} \psi_0 P_j dK \\ \int_{K_k} \psi_1 P_j dK \\ \int_{K_k} \psi_2 P_j dK \end{bmatrix}.$$

After the polynomial reconstruction is performed, an oscillation indicator is used to assess the smoothness of P_i . The oscillation indicator for the polynomial P_i , $i = 0, \dots, 8$, can be defined as $o_i = \|\nabla P_i\|$, in with $\|\cdot\|$ is the Euclidian norm. The coefficients of the new solution u in element K_k are constructed as the sum of all the polynomials multiplied by a weight, $\hat{u}_q = \sum_{i=0}^8 w_i (\hat{u}_q)_i$, $q = 0, 1, 2$, in which the weights are computed as:

$$w_i = \frac{(\epsilon + o_i(P_i))^{-\gamma}}{\sum_{j=0}^8 (\epsilon + o_j(P_j))^{-\gamma}}, \quad (17)$$

where γ is a positive number. Take ϵ small, e.g., $\epsilon = 10^{-12}$ and $\gamma = 1$. If we want more smoothing, choose e.g. $\gamma = 10$.

The discontinuity detector introduced in Krivodonova et al. [20] defines for each element \mathcal{K}_k^n a measure of the discontinuity \mathcal{I}_k . This will indicate regions where the gradient of a variable \mathcal{V} is large. For the depth-averaged two-phase flow equations, depending on the situation, we choose either $\mathcal{V} = h$ and $\mathcal{V} = \alpha$. The discontinuity detector is given by:

$$\mathcal{I}_k^n = \max(\mathcal{I}_k^n(h), \mathcal{I}_k^n(\alpha)), \quad \mathcal{I}_k^n(\mathcal{V}) = \frac{\sum_{\mathcal{S}_m \in \partial \mathcal{K}_k^n} \int_{\mathcal{S}_m} |\mathcal{V}^R - \mathcal{V}^L| d\mathcal{S}}{h_{\mathcal{K}}^{(p+1)/2} |\partial \mathcal{K}_k^n| \|\mathcal{V}\|_{\infty}}, \quad (18)$$

where $h_{\mathcal{K}}$ the cell measure defined as the radius of the largest circumscribed circle in the element \mathcal{K}_k^n , p the polynomial order, $|\partial \mathcal{K}_k^n|$ the surface area of the element and $\|\cdot\|_{\infty}$ the maximum norm. The solution is assumed to be smooth when $\mathcal{I}_k < 1$ and non-smooth when $\mathcal{I}_k > 1$.

4 Verification

4.1 Sub- and supercritical flow over a bump

We consider the 1D steady-state solution of sub- and supercritical flow over a bump [31] for both depth-averaged models A and B. This is a popular test case to verify shallow water codes [6,16,23,40,35] and we extend the test case to the depth-averaged two-phase flow models. For this test case we consider for depth-averaged model A:

$$\begin{bmatrix} h(1-\alpha) \\ h\alpha \\ h\alpha v \\ h(1-\alpha)u \\ b \end{bmatrix}_t + \begin{bmatrix} h(1-\alpha)u \\ h\alpha v \\ h\alpha v^2 + \frac{1}{2}\varepsilon(1-\rho)\varphi_{11}g_3h^2\alpha \\ h(1-\alpha)u^2 \\ 0 \end{bmatrix}_x + \begin{bmatrix} 0 & 0 & 0 & 0 & 0 \\ 0 & 0 & 0 & 0 & 0 \\ G_{31}^A & 0 & 0 & 0 & G_{35}^A \\ G_{41}^A & 0 & 0 & 0 & G_{45}^A \\ 0 & 0 & 0 & 0 & 0 \end{bmatrix} \begin{bmatrix} h \\ \alpha \\ v \\ u \\ b \end{bmatrix}_x = \begin{bmatrix} 0 \\ 0 \\ S_3^A \\ S_4^A \\ 0 \end{bmatrix}, \quad (19)$$

where

$$\begin{aligned} G_{31}^A &= \varepsilon\rho\alpha g_3h, & G_{35}^A &= \varepsilon(1-\rho)\varphi_{11}g_3h\alpha + \varepsilon\rho h\alpha g_3, \\ G_{41}^A &= \varepsilon(1-\alpha)g_3h, & G_{45}^A &= \varepsilon(1-\alpha)g_3h, \\ S_3^A &= hF^D, & S_4^A &= -hF^D/\rho. \end{aligned}$$

For depth-averaged model B we consider

$$\begin{bmatrix} h(1-\alpha) \\ h\alpha \\ h\alpha v \\ h(1-\alpha)u \\ b \end{bmatrix}_t + \begin{bmatrix} h(1-\alpha)u \\ h\alpha v \\ h\alpha v^2 + \frac{1}{2}\varepsilon(1-\rho)\varphi_{11}g_3h^2\alpha \\ h(1-\alpha)u^2 + \frac{1}{2}\varepsilon g_3h^2 \\ 0 \end{bmatrix}_x + \begin{bmatrix} 0 & 0 & 0 & 0 & 0 \\ 0 & 0 & 0 & 0 & 0 \\ 0 & 0 & 0 & 0 & G_{35}^B \\ 0 & 0 & 0 & 0 & G_{45}^B \\ 0 & 0 & 0 & 0 & 0 \end{bmatrix} \begin{bmatrix} h \\ \alpha \\ v \\ u \\ b \end{bmatrix}_x = \begin{bmatrix} 0 \\ 0 \\ S_3^B \\ S_4^B \\ 0 \end{bmatrix}, \quad (20)$$

where

$$\begin{aligned} G_{35}^B &= \varepsilon(1-\rho)\varphi_{11}g_3h\alpha, & G_{45}^B &= \varepsilon g_3h, \\ S_3^B &= hF^D/(1-\alpha), & S_4^B &= -hF^D/(\rho(1-\alpha)). \end{aligned}$$

Note that we take the given topography to be formally unknown in the system. This leads to a well-balanced scheme [31]. Let the upstream variables be denoted as h_0, α_0, u_0 and v_0 . For both the subcritical and supercritical test case we take $h_0 = 1, u_0 = 1, v_0 = 1$, and $\alpha = 0.3$.

We consider the solution on a domain $x \in [0, 1]$ in which the topography is given by [40]:

$$b(x) = \begin{cases} 0.2 - 20(x - 0.5)^2 & \text{if } 0.4 \leq x \leq 0.6, \\ 0 & \text{otherwise.} \end{cases}$$

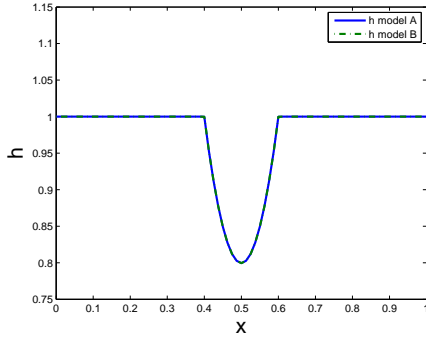
As initial condition we take $h + b = 1$, $u = u_0$, $v = v_0$ and $\alpha = \alpha_0$. At the boundaries we define the exterior trace to be the same as the initial condition. For the subcritical test case we take $g_3 = 10^8$ while for the supercritical test case $g_3 = 25$. Other parameters in the model are chosen as: $\varepsilon = 0.01$, $\rho = 0.9$, $\varphi_{11} = 2(1 - \sqrt{1 - \cos^2(\phi_{int})(1 + \tan^2(\phi_{bed}))}) / \cos^2(\phi_{int}) - 1$, $\phi_{int} = 24.5^\circ$ and $\phi_{bed} = 14.75^\circ$. In F^D , the parameters are $\rho^f = 1000 \text{ kg m}^{-3}$, $v_T = 0.143 \text{ m s}^{-1}$, $d = 10^{-3} \text{ m}$ and $\mu^f = 10^{-3} \text{ kg (ms)}^{-1}$.

We compute the order of convergence by comparing the space-time discontinuous Galerkin finite element solution of (19) and (20) to an “exact” solution of (19) and (20). This “exact” solution is found by setting the time-derivative terms in (19) and (20) to zero and we then solve the remaining systems of ODE’s with a RK45 method on a grid with 10000 points.

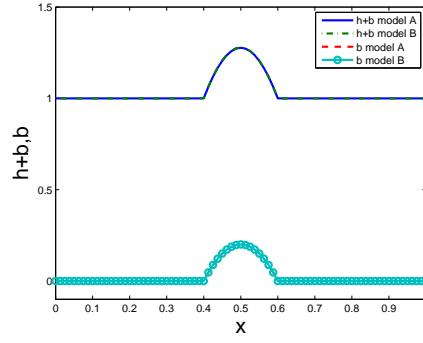
In Figure 6 we plot and compare the numerical solutions of depth-averaged models A and B of the total flow height $h + b$, topography b , flow depth h , particle volume fraction α and the velocities u and v for sub- and supercritical flow. We see that the individual variables differ for each depth-averaged model but that the mixture variables, i.e. $h = h\alpha + h(1 - \alpha)$ and $h\alpha v + \rho h(1 - \alpha)$ for both models are equal, as expected, since, as mentioned before, even though the momentum equations of the separate phases of depth-averaged models A and B are different, the mixture momentum equations are the same. The order of convergence is given in Tables 1 and 2 for sub- and supercritical flow, respectively. For a linear polynomial approximation we obtain as expected second order convergence.

4.2 Slope limiter and discontinuity detector

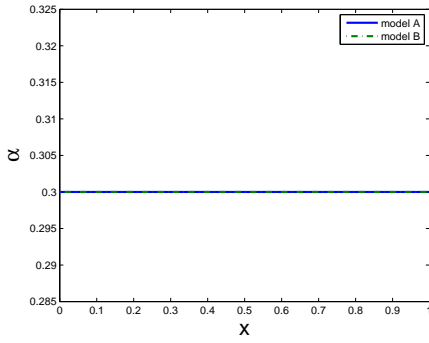
We consider a Riemann problem to test the slope limiter and the discontinuity detector in the space-time DGFEM discretization. For this test case we neglect the source terms. Furthermore, we simplify the expressions for φ_{11} , φ_{22} , φ_{12} and φ_{21} by taking $\varphi_{11} = \varphi_{22} = 1$ and $\varphi_{12} = \varphi_{21} = 0$. Other parameters in the model are chosen as $\rho = 1$, $g = 1$ and $\varepsilon = 1$. We consider the solution on a domain $[0, 1] \times [0, 1]$ divided into 32×32 elements. A physical time step of $\Delta t = 0.005$ is used and we consider the solution at final time $T = 0.4$. We



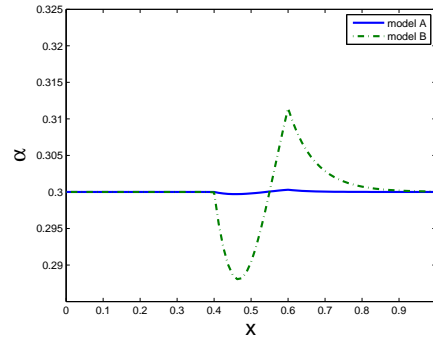
(a) Subcritical flow: flow depth h .



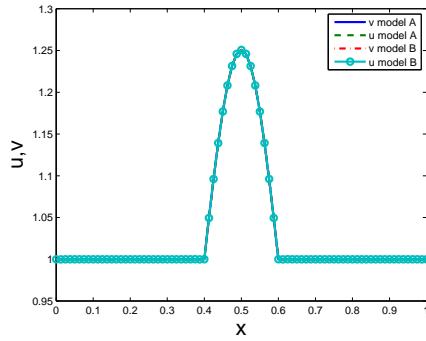
(b) Supercritical flow: flow height $h+b$ and topography b .



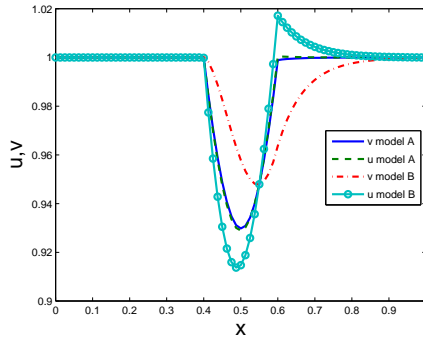
(c) Subcritical flow: particle volume fraction α .



(d) Supercritical flow: particle volume fraction α .



(e) Subcritical flow: velocities u and v .



(f) Supercritical flow: velocities u and v .

Fig. 6. Steady-state solution of depth-averaged models A and B on a grid with 80 elements.

consider the following Riemann problem:

$$V(t=0) = \begin{cases} V^L & \text{for } x < 0.5 \text{ and } y < 0.5, \\ V^R & \text{otherwise,} \end{cases}$$

N_{cells}	depth-averaged Model A				depth-averaged Model B			
	b	p	$h(\alpha v + \rho(1 - \alpha)u)$	p	b	p	$h(\alpha v + \rho(1 - \alpha)u)$	p
10	$1.5171 \cdot 10^{-2}$	-	$4.2299 \cdot 10^{-3}$	-	$1.5171 \cdot 10^{-2}$	-	$4.0809 \cdot 10^{-3}$	-
20	$3.7397 \cdot 10^{-3}$	2.0	$1.0484 \cdot 10^{-3}$	2.0	$3.7397 \cdot 10^{-3}$	2.0	$1.0340 \cdot 10^{-3}$	2.0
40	$9.3222 \cdot 10^{-4}$	2.0	$2.9977 \cdot 10^{-4}$	1.8	$9.3222 \cdot 10^{-4}$	2.0	$2.9783 \cdot 10^{-4}$	1.8
80	$2.3296 \cdot 10^{-4}$	2.0	$8.1480 \cdot 10^{-5}$	1.9	$2.3296 \cdot 10^{-4}$	2.0	$8.1175 \cdot 10^{-5}$	1.9

Table 1

Subcritical flow: L^2 error for the topography b and the total momentum $h(\alpha v + \rho(1 - \alpha)u)$ and the convergence rate p .

N_{cells}	depth-averaged Model A				depth-averaged Model B			
	b	p	$h(\alpha v + \rho(1 - \alpha)u)$	p	b	p	$h(\alpha v + \rho(1 - \alpha)u)$	p
10	$1.2910 \cdot 10^{-2}$	-	$4.0446 \cdot 10^{-4}$	-	$1.2901 \cdot 10^{-2}$	-	$4.8894 \cdot 10^{-4}$	-
20	$3.4861 \cdot 10^{-3}$	1.9	$1.4343 \cdot 10^{-4}$	1.5	$3.4861 \cdot 10^{-3}$	1.9	$1.7765 \cdot 10^{-4}$	1.5
40	$9.0211 \cdot 10^{-4}$	2.0	$3.7399 \cdot 10^{-5}$	1.9	$9.0211 \cdot 10^{-4}$	2.0	$4.7258 \cdot 10^{-5}$	1.9
80	$2.2925 \cdot 10^{-4}$	2.0	$9.4394 \cdot 10^{-6}$	2.0	$2.2925 \cdot 10^{-4}$	2.0	$1.2046 \cdot 10^{-5}$	2.0

Table 2

Supercritical flow: L^2 error for the topography b and the total momentum $h(\alpha v + \rho(1 - \alpha)u)$ and the convergence rate p .

in which V is the vector of primitive variables and $V^L = [1, 0.4, 0, 0, 0, 0]^T$ and $V^R = [0.5, 0.2, 0, 0, 0, 0]^T$. At the boundaries we set $u_1 = u_2 = v_1 = v_2 = 0$.

The slope limiter is used in element \mathcal{K}_k^n only when the discontinuity detector $\mathcal{I}_k^n > \varepsilon_{kriv}$. In this test case we take $\varepsilon_{kriv} = 1$. In (17) we take $\gamma = 1$.

In Figures 7 and 8 we compare the solutions of the volume fraction α and the flow height h computed using a slope limiter with and without the discontinuity detector for depth-averaged Model A. The results for depth-averaged model B are very similar and we do not show the figure for this model. We plot the results per element to show the discontinuities at the element faces which would not be visible with post-processing. We see that the discontinuity detector is necessary to avoid too much numerical dissipation since it prevents the limiter to be active in regions with large gradients which are not really a discontinuity. We remark that without the slope limiter it was not possible to do this test case because α became less than zero in regions around large discontinuities due to undershoots. In Figure 9 we indicate the areas where

the discontinuity detector detects large discontinuities. In these regions the slope limiter is used.

5 Validation

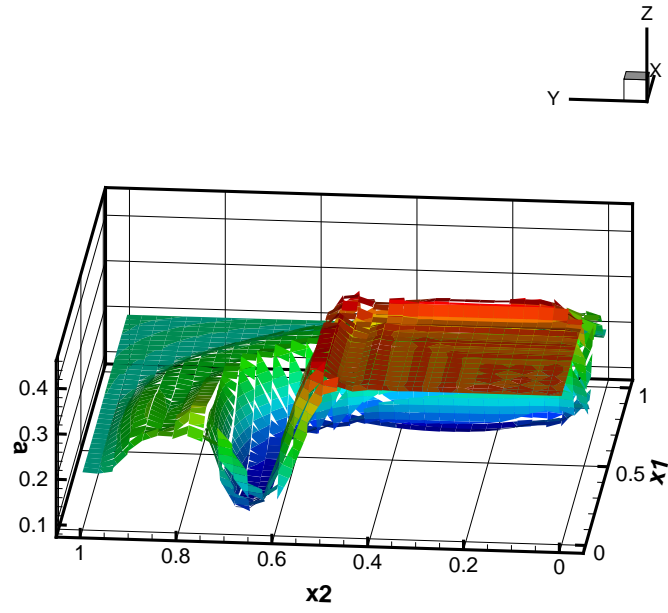
In [1,2,35] laboratory experiments of shallow water and in [38] laboratory experiments of shallow granular flow through a contraction were compared to numerical results. We will simulate a two-phase flow mixture consisting of solid particles in water in which the density of the solid particles is slightly higher than that of water. We will simulate the flow of this mixture as it enters a contraction. Initially we start with a flow with very low particle volume fraction (5 %) and the flow reaches a steady-state with oblique jumps. We then perturb this steady-state by increasing the particle volume fraction at the inlet to 30 % for a short period. This perturbation was sufficient to perturb the flow with oblique jumps to one with an upstream moving shock as was observed by Akers and Bokhove [1] (see Figure 2). We now describe the numerical setup.

In our numerical calculations we consider a channel in the cartesian coordinate system $(x, y) \in [0, 20] \times [-0.5, 0.5]$. The channel converges from $x = 8$ to $x = 10.3$ and diverges from $x = 10.3$ to $x = 15.1$. At the inflow boundary we specify the flow height, $h = 1$, the x -components of the velocities, $u_1 = 1$ and $v_1 = 1$, the y -components of the velocities, $u_2 = 0$ and $v_2 = 0$, and the particle volume fraction α . Initially, the inflow condition for the particle volume fraction is $\alpha = 0.05$. For time $30 < t < 35$ we change the inflow condition by increasing the particle volume fraction to $\alpha = 0.3$ after which we decrease the particle volume fraction again to $\alpha = 0.05$. At the walls we follow Ambati and Bokhove [3] and impose:

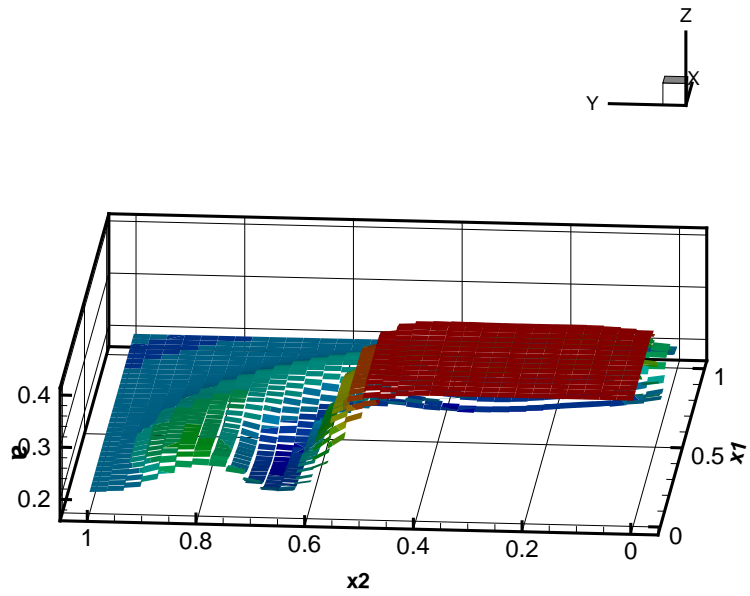
$$\begin{aligned} \mathbf{v}^b \cdot \bar{\mathbf{n}} &= -\mathbf{v}^L \cdot \bar{\mathbf{n}}, & \mathbf{v}^b \cdot \bar{\mathbf{t}} &= \mathbf{v}^L \cdot \bar{\mathbf{t}}, \\ \mathbf{u}^b \cdot \bar{\mathbf{n}} &= -\mathbf{u}^L \cdot \bar{\mathbf{n}}, & \mathbf{u}^b \cdot \bar{\mathbf{t}} &= \mathbf{u}^L \cdot \bar{\mathbf{t}}, \end{aligned} \tag{21}$$

where $\bar{\mathbf{t}}$ is the unit tangential vector orthogonal to the normal vector $\bar{\mathbf{n}}$. Furthermore, we extrapolate the void fraction, $\alpha^R = \alpha^L$ and the flow height $h^R = h^L$. At the outflow boundary, all variables are extrapolated, $U^R = U^L$. The initial condition is chosen as $h = 1$, $\alpha = 0.05$, $u_1 = v_1 = 1$ and $u_2 = v_2 = 0$.

There are a number of constants in the depth-averaged flow model. We will consider shallow liquid-solid flows with a height to length ratio of $\varepsilon = 0.01$ and for which the liquid to solid density ratio is $\rho = 0.9$. The gravity constant is $g = 9$ [1] so that the gravity components are $g_1 = \sin(\theta)g$, $g_2 = 0$ and $g_3 = \cos(\theta)g$ in which θ is the angle of the contraction with respect to the horizontal. We take $\theta = 0^\circ$ for $0 \leq x \leq 12$ and $\theta = 10^\circ$ for $x > 12$ so

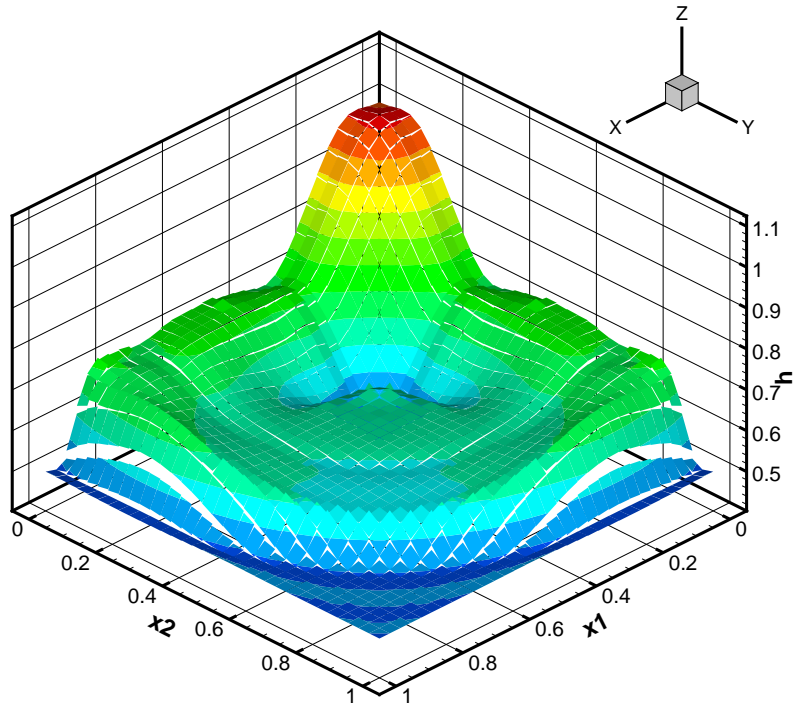


(a) With discontinuity detector and local slope limiter.

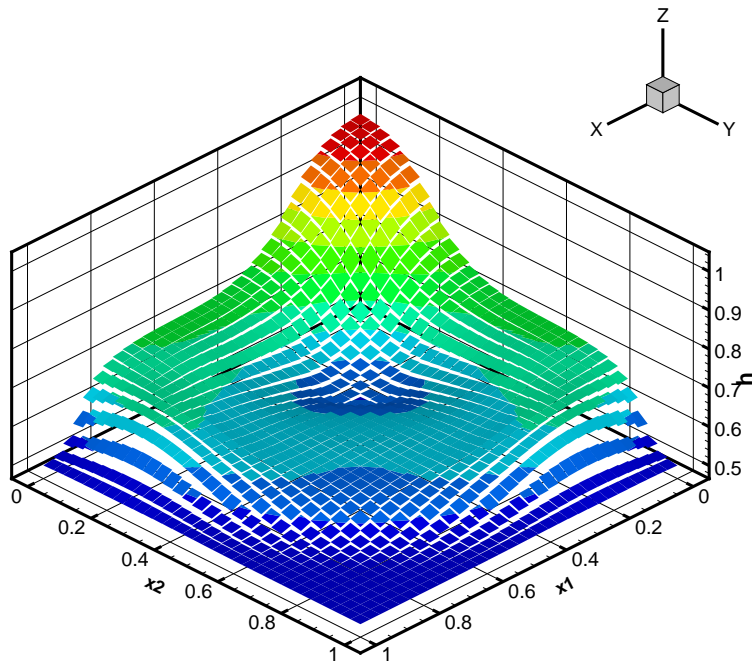


(b) Without discontinuity detector; slope limiter is used everywhere.

Fig. 7. Solution of the volume fraction α at $T = 0.37$ for depth-averaged Model A.



(a) With discontinuity detector and local slope limiter.



(b) Without discontinuity detector; slope limiter is used everywhere.

Fig. 8. Solution of the flow height h at $T = 0.37$ for depth-averaged Model A.

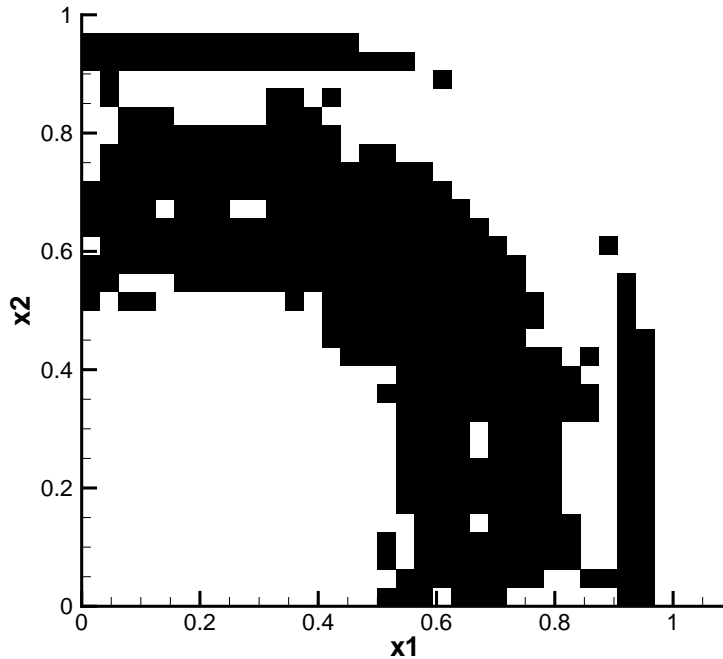


Fig. 9. The shaded area indicates where the discontinuity detector has large values and where the slope limiter is used at $T = 0.37$.

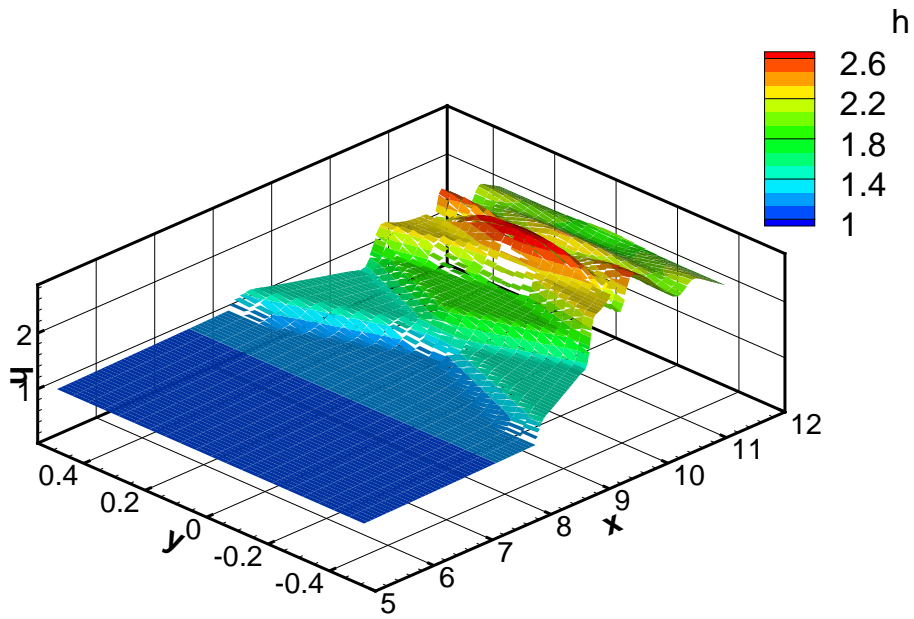
that the outflow boundary has no effect on the solution in the contraction. To be able to calculate the drag function F^D , we use the following constants: $\rho^f = 1000 \text{ kg m}^{-3}$ and $\mu^f = 10^{-3} \text{ kg (ms)}^{-1}$ while the solid particles are assumed to have a diameter of $d = 10^{-3} \text{ m}$ and $v_T = 0.143 \text{ m s}^{-1}$ [18]. The internal angle of friction is taken to be $\phi_{int} = 24.5^\circ$ and the bed friction angle is $\phi_{bed} = 14.75^\circ$ [4]. The bottom topography is taken constant $b(x, y) = 0$.

We compute the solution for the depth-averaged models A and B using space DGFEM until $t = 80$ using a CFL number of $\text{CFL} = 0.8$ on a grid with 300 elements in the x -direction and 20 elements in the y -direction. In Figures 10- 12 we show the transition of the flow height h from oblique jumps to an upstream moving shock as calculated with depth-averaged Model A (for a comparison, see also Figure 2). We see the same as observed by Akers and Bokhove [1] that after perturbing the steady-state solution of oblique jumps, an upstream moving shock appears. To compare the results of depth-averaged models A and B, we compare in Figure 13 the flow height h and particle volume fraction α of both models along the centre line $y = 0$. We see, as before, that the particle volume fraction α for the depth-averaged models A and B differ, but that the mixed variable $h = h\alpha + h(1 - \alpha)$ for both models are nearly the same. We can conclude that although depth-averaged models A and B give different results for the separate components of

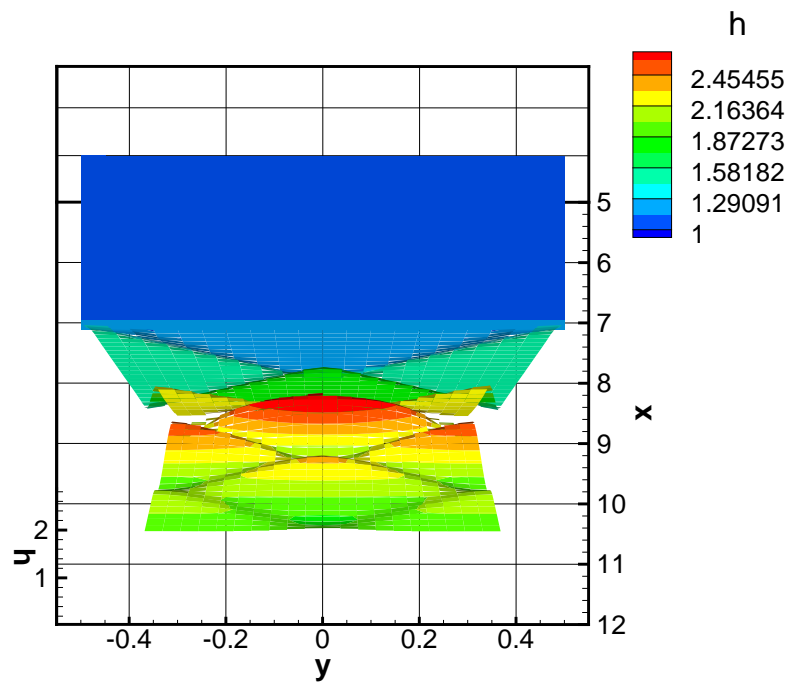
$U = [h(1 - \alpha), h\alpha, h\alpha v_i, h(1 - \alpha)u_i]^T$, both models give the same results for the mixture components h and $h(\alpha v_i + \rho(1 - \alpha)u_i)$. Furthermore, note that the position of the hydraulic jump in Figures 13a, c and e is exactly the same for the model with nonconservative products (model A) and the model in conservative form (model B). This shows the ability of the discontinuous Galerkin finite element method for nonconservative products, as developed in [31], to well capture shocks and that for this test case it does not matter how the path $\phi(\tau; U_L, U_R)$ in the weak formulation (7) is chosen.

6 Conclusions

Recently, a depth-averaged two-phase flow model was introduced by Pitman and Le [29] and Le [22] to model shallow debris flows. This model contains non-conservative products which makes it numerically challenging to solve. In Riebergen et al. [31] we developed a discontinuous Galerkin finite element method to deal with nonconservative products which we applied in this article to solve the depth-averaged two-phase flow model of Le [22]. We also introduced a new depth-averaged two-phase flow model in this article which does not contain nonconservative products and for which standard numerical methods can be applied. The DGFEM discretizations for both models were verified against steady-state flow solutions over a bump and we obtained second order convergence when using linear polynomial approximations. To prevent numerical oscillations, the WENO slope limiter [25] in combination with Krivodonova's discontinuity detector [20] was successfully applied. A Riemann problem solution was shown which could not be solved without the slope limiter due to severe undershoots. Furthermore, the effect of Krivodonova's discontinuity detector was shown. The solution of the Riemann problem was smoothed out too much if the discontinuity detector was not used. Finally, we compared numerical results of both models for shallow two-phase flows through a contraction and we qualitatively validated the models by showing the ability of the models to capture the phenomenon in which a steady state solution with oblique jumps is perturbed, by an increase of particles for a short period in time, so that an upstream moving shock appeared, as was observed by Akers and Bokhove [1]. We saw in the numerical test cases that although the individual components for both models differ, the mixture variables are the same. Depth-averaged model B has the advantage though that it is hyperbolic for a larger range of parameters than depth-averaged model A. Furthermore, we saw that the position of the hydraulic jumps as computed with depth-averaged model A, which has nonconservative products, is the same as the position of the hydraulic jumps as computed with depth-averaged model B, which can be written in conservative form. This shows the ability of the discontinuous Galerkin finite element method for nonconservative products, as developed

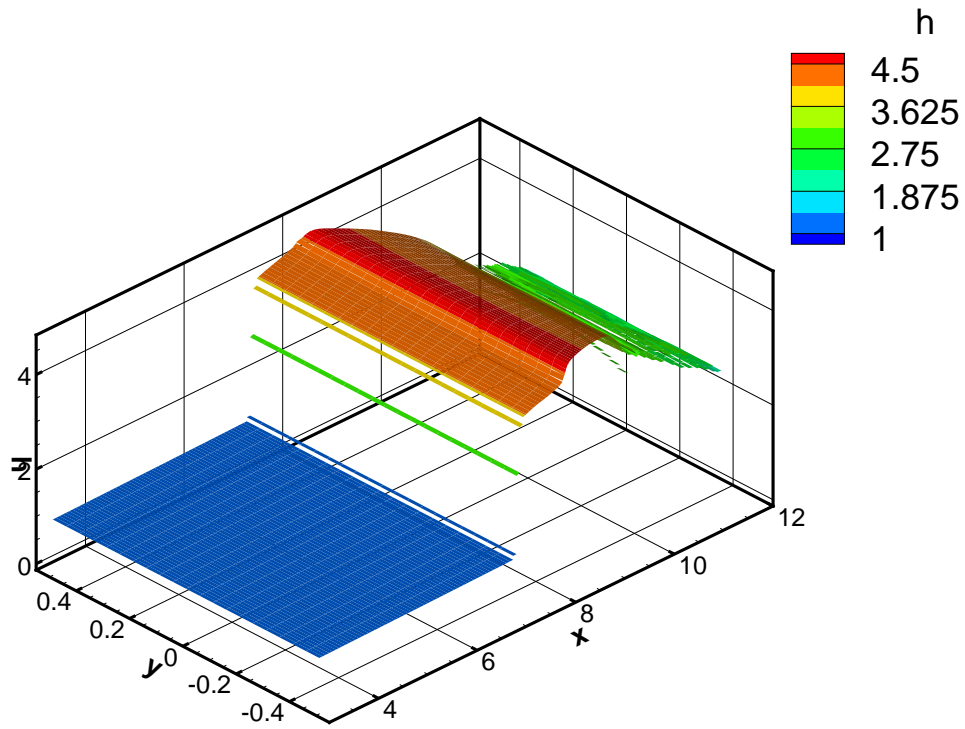


(a) Side view.

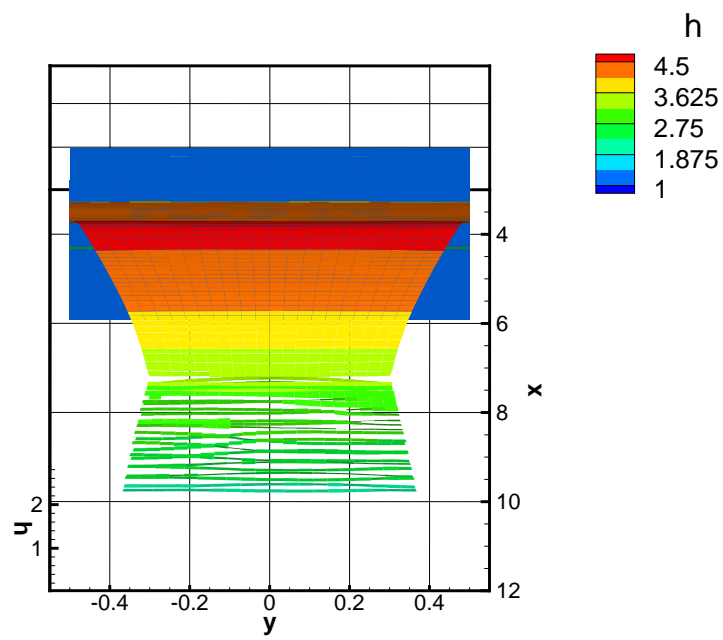


(b) Top view.

Fig. 10. Oblique jump solution at $t = 30$. Compare to the top left picture in Figure 2.

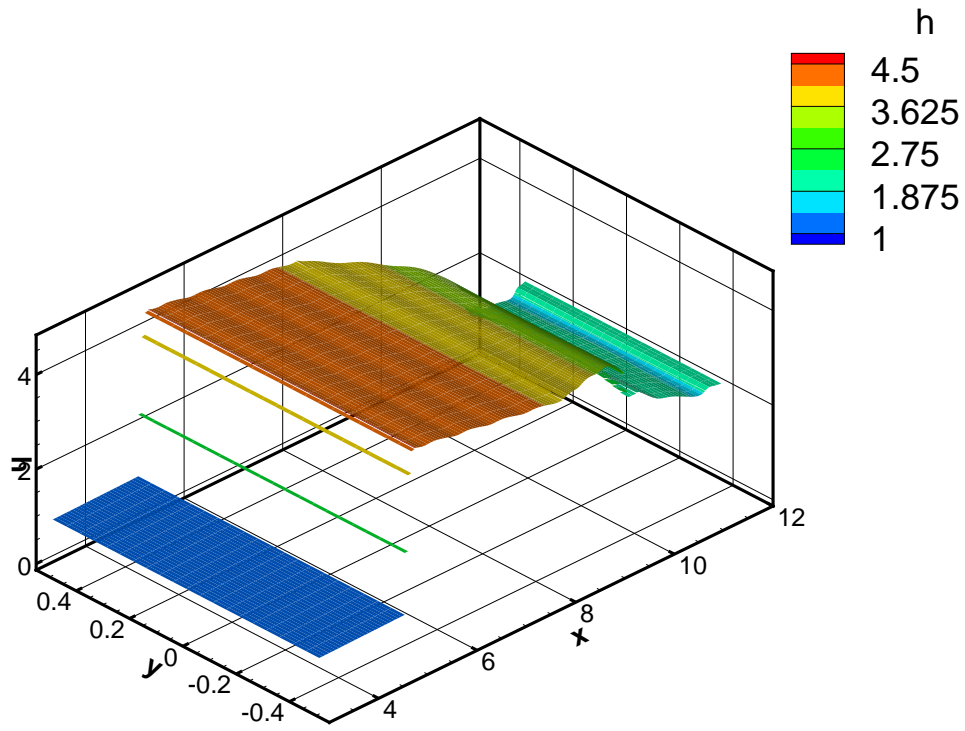


(a) Side view.

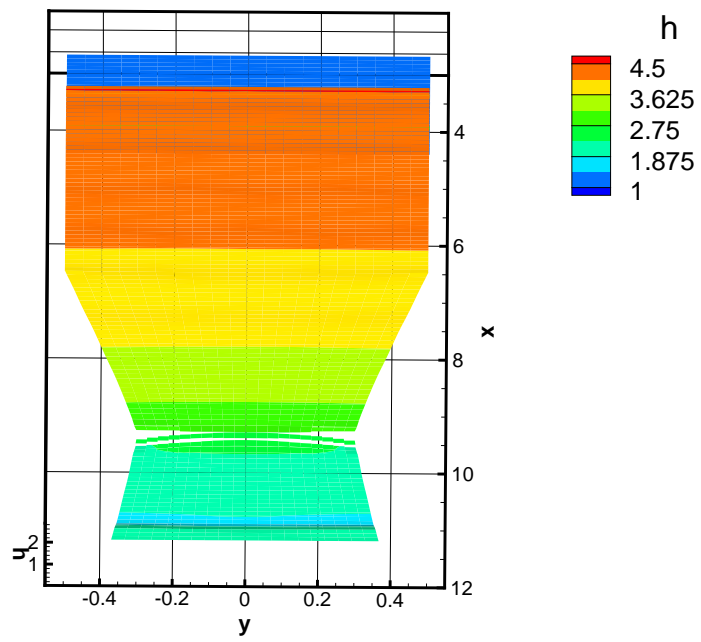


(b) Top view.

Fig. 11. Transition phase at $t = 55$. Compare with the bottom left picture in Figure 2.

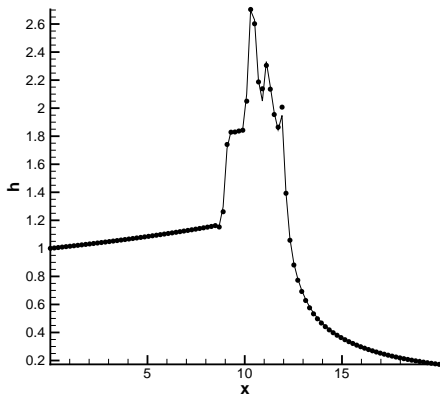


(a) Side view.

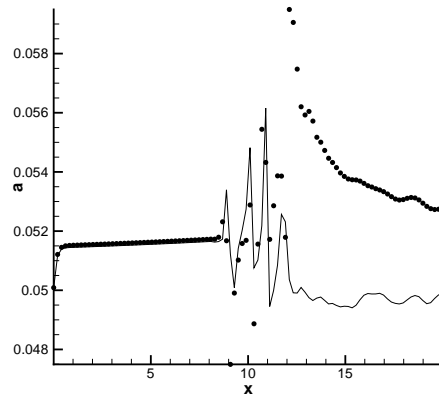


(b) Top view.

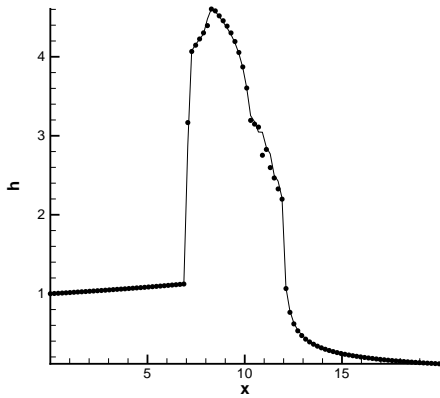
Fig. 12. Upstream moving shock at $t = 80$. Compare to the bottom right picture in Figure 2.



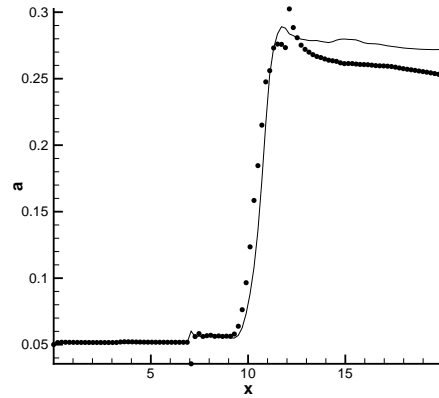
(a) Flow height h at $t = 30$.



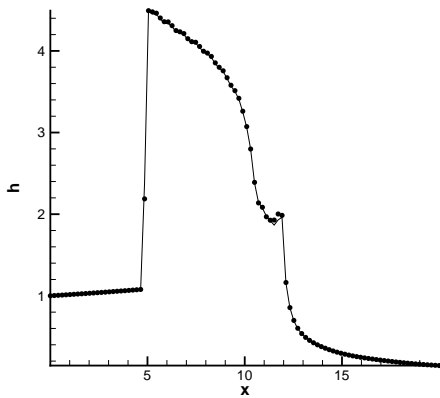
(b) Particle volume fraction α at $t = 30$.



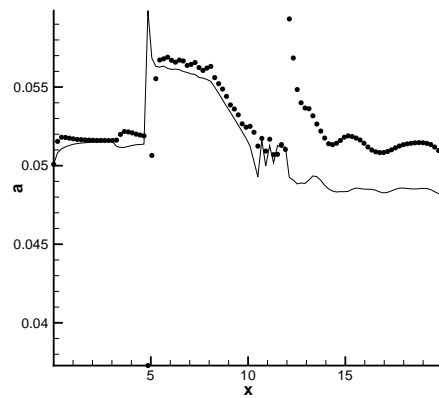
(c) Flow height h at $t = 55$.



(d) Particle volume fraction α at $t = 55$.



(e) Flow height h at $t = 80$.



(f) Particle volume fraction α at $t = 80$.

Fig. 13. Comparing the solution of the flow height h and particle volume fraction α along the centre line $y = 0$ as calculated with depth-averaged models A and B during the transition from oblique jumps to an upstream moving shock. The solid lines are the solutions calculated with depth-averaged Model A while the dots are the solutions calculated with depth-averaged Model B. The contraction is from $x = 8$ to $x = 15.1$.

in [31], to well capture shocks and that for this test case it does not matter how the path $\phi(\tau; U_L, U_R)$ in the weak formulation (7) is chosen.

Acknowledgments

S.R. and O.B. acknowledge support from the Institute of Mechanics, Processes and Control Twente. For J.V. this research was partly funded by the ICT project BRICKS (<http://www.bsik-bricks.nl>), theme MSV1. Furthermore, we would like to thank Henk Sollie for discussions on the slope limiter and Vijaya Ambati for proofreading.

A Models A and B

In this section we will compare Models A and B. We assume that the only fluids stress is the fluids pressure. Furthermore, the densities ρ^f and ρ^s of both phases are assumed to be constant. Models A and B consist of two continuity equations and two momentum equations. The continuity equations of both models are the same and are given by:

$$\begin{aligned}\partial_t((1 - \alpha)) + \partial_k((1 - \alpha)u_k) &= 0, \\ \partial_t(\alpha) + \partial_k(\alpha v_k) &= 0.\end{aligned}\tag{A.1}$$

The momentum equations for Model A are given by:

$$\begin{aligned}\partial_t((1 - \alpha)\rho^f u_i) + \partial_k((1 - \alpha)\rho^f u_i u_k) &= -(1 - \alpha)\partial_k(\delta_{ik}p^f) - F_i^D + (1 - \alpha)\rho^f g_i, \\ \partial_t(\alpha\rho^s v_i) + \partial_k(\alpha\rho^s v_i v_k + T_{ik}^s) &= -\alpha\partial_k(\delta_{ik}p^f) + F_i^D + \alpha\rho^s g_i,\end{aligned}\tag{A.2}$$

while the momentum equations for Model B are given by:

$$\begin{aligned}\partial_t((1 - \alpha)\rho^f u_i) + \partial_k((1 - \alpha)\rho^f u_i u_k + \delta_{ik}p^f) &= -F_i^D/(1 - \alpha) + \rho^f g_i, \\ \partial_t(\alpha\rho^s v_i) + \partial_k(\alpha\rho^s v_i v_k + T_{ik}^s) &= F_i^D/(1 - \alpha) + (\rho^s - \rho^f)\alpha g_i.\end{aligned}\tag{A.3}$$

In these equations α is the particle volume fraction, u the fluid velocity vector, v the solids velocity vector, g the gravity vector, T^s the solids stress tensor and F^D the generalized drag force. Note that Model B does not have non-conservative products and that there is no fluid pressure term present in the momentum equation for the solids phase. This is the case in Model A. We remark, however, that although the momentum equations for the separate phases are different, the mixture momentum equations, obtained by adding

the momentum equations of the separate phases, for both models are the same. As mentioned by Gidaspow [14], the models can be expected to give different values of the relative velocity only and not for the average mixture quantities.

References

- [1] B. Akers and O. Bokhove, Hydraulic flow through a channel contraction: Multiple steady states, *Phys. Fluids*, 20 (2008) 056601.
- [2] V.R. Ambati and O. Bokhove, Space-time discontinuous Galerkin finite element method for shallow water flows, *J. Comput. Appl. Math.* 204 (2007) 452.
- [3] V.R. Ambati and O. Bokhove, Space-time discontinuous Galerkin discretization of rotating shallow water equations, *J. Comput. Phys.* 225 (2007) 1233.
- [4] N.J. Balmforth and R.R. Kerswell, Granular collapse in two dimensions, *J. Fluid Mech.* 538 (2005) 399.
- [5] A. Boemer, H. Qi and U. Renz, Eulerian simulation of bubble formation at a jet in a two-dimensional fluidized bed, *Int. J. Multiphase Flow* 23 (1997) 927.
- [6] M. Castro, J.M. Gallardo and C. Parés, High order finite volume schemes based on reconstruction of states for solving hyperbolic systems with nonconservative products. Application to shallow-water systems, *Math. Comput.* 75 (2006) 1103.
- [7] M.-C. Chiou, Y. Wang and K. Hutter, Influence of obstacles on rapid granular flows, *Acta Mechanica* 175 (2005) 105.
- [8] B. Cockburn and C.W. Shu, The Runge-Kutta discontinuous Galerkin method for conservation laws V, *J. Comput. Phys.* 141 (1998) 199.
- [9] G. Dal Maso, P.G. LeFloch and F. Murat, Definition and weak stability of nonconservative products, *J. Math. Pures Appl.* 74 (1995) 483.
- [10] R.P. Denlinger and R.M. Iverson, Flow of variably fluidized granular masses across three-dimensional terrain 2. Numerical predictions and experimental tests, *J. Geophys. Res.* 106 (2001) 553.
- [11] D.A. Drew and R.T. Lahey, Analytical modeling of multiphase flow, in *Particulate Two-Phase flows*, edited by M.C. Roco, Butterworth-Heinemann, Boston, 1993
- [12] D.A. Drew and S.L. Passman, *Theory of multicomponent fluids*, Springer, 1999
- [13] H. Enwald, E. Peirano and A.E. Almstedt, Eulerian Two-phase Flow Theory Applied to Fluidization, *Int. J. Multiphase Flow* 22 (1996) 21.
- [14] D. Gidaspow, *Multiphase flow and fluidization*, Academic Press, 1994
- [15] J.M.N.T. Gray, Y.-C. Tai and S. Noelle, Shock waves, dead zones and particle-free regions in rapid granular free-surface flows, *J. Fluid Mech.* 491 (2003) 161.

- [16] D.D. Houghton and A. Kasahara, Nonlinear Shallow Fluid Flow Over an Isolated Ridge, *Comm. on Pure and Applied Math.* 21 (1968) 1.
- [17] R.M. Iverson and R.P. Denlinger, Flow of variably fluidized granular masses across three-dimensional terrain 1. Coulomb mixture theory, *J. Geophys. Res.* 106 (2001) 537.
- [18] R. Jackson, *The dynamics of fluidized particles*, Cambridge University Press, 2000
- [19] C.M. Klaij, J.J.W. van der Vegt and H. van der Ven, Space-time discontinuous Galerkin method for the compressible Navier-Stokes equations, *J. Comput. Phys.* 217 (2006) 589.
- [20] L. Krivodonova, J. Xin, J.F. Remacle, N. Chevaugeon and J.E. Flaherty, Shock detection and limiting with discontinuous Galerkin methods for hyperbolic conservation laws, *Appl. Numer. Math.* 48 (2004) 323.
- [21] <http://www.nsm.buffalo.edu/~astinton>
- [22] L.H. Le, *New models for geophysical flows*, Ph. D. dissertation, State University of New York at Buffalo, 2006.
- [23] R.J. LeVeque, Balancing source terms and flux gradients in high-resolution Godunov methods: the quasi-steady wave-propagation algorithm, *J. Comput. Phys.*, 146 (1998) 346.
- [24] J. Ling, P.V. Skudarnov, C.X. Lin and M.A. Ebadian, Numerical investigations of liquid-solid slurry flows in a fully developed turbulent flow region, *International Journal of Heat and Fluid Flow* 24 (2003) 389.
- [25] H. Luo, J.D. Baum and R. Löhner, A Hermite WENO-based limiter for discontinuous Galerkin method on unstructured grids, *J. Comput. Phys.* 225 (2007) 686.
- [26] J.J. Major and R.M. Iverson, Debris-flow deposition: Effects of pore-fluid pressure and friction concentrated at flow margins, *GSA Bulletin* 111 (1999) 1424.
- [27] A.K. Patra, C.C. Nichita, A.C. Bauer, E.B. Pitman, M. Bursik and M.F. Sheridan, Parallel adaptive discontinuous Galerkin approximation for thin layer avalanche modeling, submitted to *Computers and Geosciences* (2004).
- [28] A.K. Patra, A.C. Bauer, C.C. Nichita, E.B. Pitman, M.F. Sheridan, M. Bursik, B. Rupp, A. Webber, A.J. Stinton, L.M. Namikawa and C.S. Renschler, Parallel adaptive numerical simulation of dry avalanches over natural terrain, *J. Volc. Geothermal Research* 139 (2005) 1.
- [29] E.B. Pitman and L. Le, A two-fluid model for avalanche and debris flows, *Phi. Trans. R. Soc. A* 363 (2005) 1573.
- [30] O. Pouliquen and Y. Forterre, Friction law for dense granular flows: application to the motion of a mass down a rough inclined plane, *J. Fluid Mech.* 453 (2002) 133.

- [31] S. Rhebergen, O. Bokhove and J.J.W. van der Vegt, Discontinuous Galerkin finite element methods for hyperbolic nonconservative partial differential equations, *J. Comput. Phys.* 227 (2008) 1887.
- [32] S.B. Savage and K. Hutter, The dynamics of avalanches of granular materials down a rough incline, *J. Fluid Mech.* 199 (1989) 177.
- [33] <http://www.liceng.dk/LIC/Services/SlurryAndSediment/index.shtml>
- [34] Y.C. Tai, S. Noelle, J.M.N.T. Gray and K. Hutter, Shock-capturing and front-tracking methods for granular avalanches, *J. Comput. Phys* 175 (2002) 269.
- [35] P.A. Tassi, O. Bokhove and C.A. Vionnet, Space discontinuous Galerkin method for shallow water flows - kinetic and HLLC flux, and potential vorticity generation, *Adv. Water Resour.* 30 (2007) 998.
- [36] E.F. Toro, *Riemann solvers and numerical methods for fluid dynamics*, Springer Verlag, 1997.
- [37] J.J.W. van der Vegt and H. van der Ven, Space-Time Discontinuous Galerkin Finite Element Method with Dynamic Grid Motion for Inviscid Compressible Flows I. General Formulation, *J. Comput. Phys.* 182 (2002) 546.
- [38] A.W. Vreman, M. Al-Tarazi, J.A.M. Kuipers, M. van Sint Annaland and O. Bokhove, Supercritical shallow granular flow through a contraction, experiment, theory and simulation, *J. Fluid Mech.* 578 (2007) 233.
- [39] Y. Wang, K. Hutter and S.P. Pudasaini, The Savage-Hutter theory: A system of partial differential equations for avalanche flows of snow, debris and mud, *Z. Angew. Math. Mech.* 84 (2004) 507.
- [40] Y. Xing and C.W. Shu, High order well-balanced finite volume WENO schemes and discontinuous Galerkin methods for a class of hyperbolic systems with source terms, *J. Comput. Phys.* 214 (2006) 567.